Pre-supernova Evolution and Nucleosynthesis in Massive Stars and Their Stellar Wind Contribution

72

Raphael Hirschi

Abstract

In this chapter, we review the modelling and pre-supernova evolution of massive stars with a particular emphasis on the effects of rotation and mass loss. We then present the stellar wind contribution to nucleosynthesis and the production of weak s-process at various metallicities (Z). We also review the transition between intermediate-mass and massive stars and the major nuclear and stellar uncertainties involved. Rotation and mass loss both have a strong impact on the evolution and nucleosynthesis in massive stars. The effects of rotation on pre-supernova models are most spectacular for stars between 15 and 25 $M_{\odot}$. For $M > 30 M_{\odot}$, mass loss dominates over the effects of rotation. Massive stars near solar metallicity lose more than half their initial mass for stars more massive than 20 $M_{\odot}$. The stellar wind contribution to nucleosynthesis consists mostly of hydrogen-burning products and to a smaller extent helium-burning products since mass loss is generally small during the advanced phases.

At low and very low Z, one expects mass loss and the production of secondary elements like ^{14}N to decrease and gradually become negligible. Rotation changes this picture. For the most massive stars ($M \gtrsim 60 M_{\odot}$), primary production of CNO elements raises the overall metallicity of the surface drastically, and significant mass loss may occur during the red supergiant stage. The production of primary ^{14}N and also ^{22}Ne in rotating massive stars at low Z opens the door to

---

R. Hirschi (✉)
Astrophysics Group, School of Chemical and Physical Sciences, Keele University, Staffordshire, UK

Kavli Institute for the Physics and Mathematics of the Universe (WPI), University of Tokyo, Kashiwa, Chiba, Japan

UK Network for Bridging Disciplines of Galactic Chemical Evolution (BRIDGCE), Staffordshire, UK
e-mail: r.hirschi@keele.ac.uk

A.W. Alsabti, P. Murdin (eds.), *Handbook of Supernovae*,
https://doi.org/10.1007/978-3-319-21846-5_82

produce s-process elements at low Z. The strong dependence of the production of the barium peak on metallicity and initial rotation rate means that rotating models provide a natural explanation for the observed scatter in the strontium over barium ratio ([Sr/Ba]) at low metallicities.

Contents

1 Introduction 1880
2 Stellar Evolution Models 1881
  2.1 Stellar Structure Equations 1881
  2.2 Mass Loss 1883
  2.3 Rotation and Magnetic Fields 1884
3 Evolution of Massive Stars and Key Abundances 1890
  3.1 Evolution of Surface Properties (HR Diagram) and Lifetimes 1890
  3.2 Evolution of Central Properties in the Log T_c–Log ρ_c Diagram 1891
  3.3 Angular Velocity, Ω, and Momentum, j, Evolution 1895
  3.4 Structure and Abundance Evolution and Pre-supernova Properties 1896
  3.5 Abundances Evolution 1898
  3.6 Pre–supernova Properties 1901
4 Stellar Wind Contribution to Galactic Chemical Enrichment 1903
  4.1 Comparison Between Rotating and Non-rotating Models and Convolution with the IMF 1904
5 Dependence on Metallicity 1905
  5.1 Metallicity Effects on General Evolution 1905
  5.2 Effects of Rotation at Subsolar Metallicities 1906
6 Weak s-Process 1909
  6.1 Standard Weak s-Process in (Nonrotating) Massive Stars 1911
  6.2 Impact of Rotation on the s-Process 1915
7 Conclusions 1920
8 Cross-References 1923
References 1923

1 Introduction

Massive stars play a key role in the universe through the light they shine, their energetic death, and the chemical elements they produce. Indeed, the most massive stars known to exist have a luminosity roughly ten million times larger than that of our sun (Crowther et al. 2010). Their very strong radiation field leads to strong mass loss. Thus massive stars near solar metallicity ($Z_\odot$) lose a large fraction of their initial mass, more than half their initial mass for stars more massive than 20 $M_\odot$. Most of the mass loss takes place during hydrogen- and helium-burning phases. This implies that the stellar wind contribution to nucleosynthesis consists mostly of hydrogen-burning products and to a smaller extent helium-burning products, i.e., elements up to aluminum. Observations from the Integral gamma-ray satellite (Diehl et al. 2006) confirm that massive stars in our galaxy produce significant amounts of ^{26}Al, a radioactive element with half-life of $\sim 7.2 \times 10^5$ years and emitting photons at 1808.65 keV. Following helium burning, massive stars go through four additional burning stages: carbon, neon, oxygen, and silicon. During these phases, they produce elements up to iron via mainly fusion, alpha-particle capture (and photo-disintegration) reactions. Weak interactions play a increasing role as evolution proceeds and are key to reduce the electron fraction for the iron core to collapse (Arnett and Thielemann 1985; Chieffi et al. 1998; Thielemann and Arnett 1985). Massive stars produce elements heavier than iron via neutron captures during helium and carbon burning, the so-called weak s-process since the production generally stops at the first peak (strontium-zirconium).

This chapter is organized as follows. Section 2 reviews the stellar structure equations and physical ingredients of stellar evolution models. Section 3 reviews the general evolution of the massive stars as well as that of the main elements (H, He, C, N, O, …). Section 4 reviews the mass loss history and describes the stellar winds contribution to nucleosynthesis. Section 5 discusses the metallicity dependence of the evolution and nucleosynthesis of massive stars. Section 6 presents comprehensive weak s-process nucleosynthesis calculations at various metallicities. Most sections also discuss the evolution and effects of rotation. The reader is also referred to the review by Langer (2012) concerning the evolution of binary stars.

2 Stellar Evolution Models

Stellar evolution models require a wide range of input physics ranging from nuclear reaction rates to mass loss prescriptions. In this section, we review the basic equations that govern the structure and evolution of stars as well as some of the key input physics with a special emphasis on mass loss, rotation, and magnetic fields.

2.1 Stellar Structure Equations

There are four equations describing the evolution of the structure of stars: the mass, momentum, and energy conservation equations and the energy transport equation, which we recall below. On top of that, the equations of the evolution of chemical elements abundances and angular momentum are to be followed. These equations are discussed in Sect. 2.3. In the Geneva stellar evolution code (GENEC; see Eggenberger et al. 2007), which we base our presentation on in this section, the problem is treated in one dimension (1D) and the equations of the evolution of chemical elements abundances are calculated separately from the structure equations, as in the original version of Kippenhahn and Weigert (Kippenhahn and Weigert 1990; Kippenhahn et al. 1967). In GENEC, rotation is included, and spherical symmetry is no longer assumed. The effective gravity (sum of the centrifugal force and gravity) can in fact no longer be derived from a potential, and the case is said to be nonconservative. The problem can still be treated in 1D by assuming that the angular velocity is constant on isobars. This assumes that there is a strong horizontal (along isobars) turbulence which enforces constant angular velocity on isobars (Zahn 1992). The case is referred to as "shellular" rotation, and using reasonable simplifications described in Meynet and Maeder (1997), the usual set of four structure equations (as used for non-rotating stellar models) can be recovered:

- Energy conservation:

$$\frac{\partial L_P}{\partial M_P} = \varepsilon_{nucl} - \varepsilon_\nu + \varepsilon_{grav} = \varepsilon_{nucl} - \varepsilon_\nu - c_P \frac{\partial \overline{T}}{\partial t} + \frac{\delta}{\overline{\rho}} \frac{\partial P}{\partial t} \tag{1}$$

  where L_P is the luminosity, M_P the Lagrangian mass coordinate, and ε_{nucl}, ε_ν, and ε_{grav} are the energy generation rates per unit mass for nuclear reactions, neutrinos, and gravitational energy changes due to contraction or expansion, respectively. T is the temperature, c_P the specific heat at constant pressure, t the time, P the pressure, ρ the density, and $\delta = -\partial \ln\rho/\partial \ln T$.
- Momentum equation:

$$\frac{\partial P}{\partial M_P} = -\frac{GM_P}{4\pi r_P^4} f_P \tag{2}$$

  where r_P is the radius of the shell enclosing mass M_P and G the gravitational constant.
- Mass conservation (continuity equation):

$$\frac{\partial r_P}{\partial M_P} = \frac{1}{4\pi r_P^2 \overline{\rho}} \tag{3}$$

- Energy transport equation:

$$\frac{\partial \ln \overline{T}}{\partial M_P} = -\frac{GM_P}{4\pi r_P^4 P} f_P \min[\nabla_{\rm ad}, \nabla_{\rm rad} \frac{f_T}{f_P}] \tag{4}$$

where

$$\nabla_{\rm ad} = \left(\frac{\partial \ln \overline{T}}{\partial \ln P}\right)_{\rm ad} = \frac{P\delta}{\overline{T}\overline{\rho} c_P} \text{ (convective zones)},$$

$$\nabla_{\rm rad} = \frac{3}{64\pi\sigma G} \frac{\kappa L_P P}{M_P \overline{T}^4} \text{ (radiative zones)},$$

where κ is the total opacity and σ is the Stefan–Boltzmann constant.

$$f_P = \frac{4\pi r_P^4}{GM_P S_P} \frac{1}{< g^{-1} >},$$

$$f_T = \left(\frac{4\pi r_P^2}{S_P}\right)^2 \frac{1}{< g >< g^{-1} >},$$

$< x >$ is x averaged on an isobaric surface, $\overline{x}$ is x averaged in the volume separating two successive isobars, and the index P refers to the isobar with a pressure equal to P. g is the effective gravity and S_P is the surface of the isobar (see Meynet and Maeder 1997, for more details). The implementation of the structure equations into other stellar evolution codes is presented, for example, in Paxton et al. (2011) and Chieffi et al. (1998).

2.2 Mass Loss

Mass loss strongly affects the evolution of massive stars, especially for stars more massive than 30 $M_\odot$, as we shall describe below. We recall here the different mass loss prescriptions used in stellar evolution calculations and how they relate to each other. In the models presented in this chapter, the following prescriptions were used. For main-sequence stars, the prescription for radiative line-driven winds from Vink et al. (2001) was used. For stars in a domain not covered by the Vink et al. prescription, the de Jager et al. (1988) prescription was applied to models with $\log(T_{\rm eff}) > 3.7$. For $\log(T_{\rm eff}) \leq 3.7$, a linear fit to the data from Sylvester et al. (1998) and van Loon et al. (1999) (see Crowther 2001) was performed. The formula used is given in Eq. 2.1 in Bennett et al. (2012). For cool stars, dust and pulsation most probably play a role in the driving of the wind, but the driving mechanism is not fully understood.

In stellar evolution simulations, the stellar wind is not simulated self-consistently, and a criterion is used to determine when a star becomes a WR star. Usually, a star is considered to become a WR when the surface hydrogen mass fraction, X_s, becomes inferior to 0.3 (sometimes when it is inferior to 0.4) and the effective temperature, $\log(T_{\rm eff})$, is greater than 4.0. The mass loss rate used during the WR phase depends on the WR subtype. For the eWNL phase (when $0.3 > X_s > 0.05$), the Gräfener and Hamann (2008) recipe was used (in the validity domain of this prescription, which usually covers most of the eWNL phase). In many cases, the WR mass loss rate of Gräfener and Hamann (2008) is lower than the rate of Vink et al. (2001), in which case, the latter was used. For the eWNE phase – when $0.05 > X_s$ and the ratio of the mass fractions of $(^{12}\mathrm{C} + {}^{16}\mathrm{O})/^{4}\mathrm{He} < 0.03$ – and WC/WO phases, when $(^{12}\mathrm{C} + {}^{16}\mathrm{O})/^{4}\mathrm{He} > 0.03$, the corresponding prescriptions of Nugis and Lamers (2000) were used. Note also that both the Nugis and Lamers (2000) and Gräfener and Hamann (2008) mass loss rates account for clumping effects (Muijres et al. 2011).

The mass loss rates from Nugis and Lamers (2000) for the eWNE phase are much larger than in other phases, and thus the largest mass loss occurs during this phase. In Crowther et al. (2010), the mass loss prescription from Nugis and Lamers (2000) was used for both the eWNL and eWNE phases (with a clumping factor, $f = 0.1$).

More recent models, such as those of Yusof et al. (2013), thus lose less mass than those presented in Crowther et al. (2010) during the eWNL phase.

The metallicity dependence of the mass loss rates is commonly included in the following way. The mass loss rate used at a given metallicity, $\dot{M}(Z)$, is the mass loss rate at solar metallicity, $\dot{M}(Z_{\odot})$, multiplied by the ratio of the metallicities to the power of α: $\dot{M}(Z) = \dot{M}(Z_{\odot})(Z/Z_{\odot})^{\alpha}$. α was set to 0.85 for the O-type phase and WN phase and 0.66 for the WC and WO phases; and for WR stars, the initial metallicity rather than the actual surface metallicity was used in the equation above following Eldridge and Vink (2006). α was set to 0.5 for the de Jager et al. (1988) prescription.

For rotating models, the correction factor described below in Eq. 5 is applied to the radiative mass loss rate. Line-driven wind mass loss rates in hot stars are relatively well determined and constrained by observations (Crowther et al. 2010; Muijres et al. 2011). On the other hand, the mass loss rates for red supergiants and luminous blue variables as well as their metallicity dependence are not fully understood and still very uncertain with unfortunately little hope for major improvements in the near future. We will come back to this point when we discuss the metallicity dependence in Sect. 5.

2.3 Rotation and Magnetic Fields

The physics of rotation included in stellar evolution codes has been developed extensively over the last 20 years. A recent review of this development can be found in Maeder and Meynet (2012). The effects induced by rotation can be divided into three categories.

(1) **Hydrostatic effects**: The centrifugal force changes the hydrostatic equilibrium of the star. The star becomes oblate, and the equations describing the stellar structure have to be modified as described above.

(2) **Mass loss enhancement and anisotropy**: Mass loss depends on the opacity and the effective gravity (sum of gravity and centrifugal force) at the surface. The larger the opacity, the larger the mass loss. The higher the effective gravity, the higher the radiative flux (von Zeipel 1924) and effective temperature. Rotation, via the centrifugal force, reduces the surface effective gravity at the equator compared to the pole. As a result, the radiative flux of the star is larger at the pole than at the equator. In massive hot stars, since the opacity is dominated by the temperature-independent electron scattering, rotation enhances mass loss at the pole. If the opacity increases when the temperature decreases (in cooler stars), mass loss can be enhanced at the equator when the bistability is reached (Vink et al. 2001).

For rotating models, the mass loss rates can be obtained by applying a correction factor to the radiative mass loss rate as described in Maeder and Meynet (2000):

$$\dot{M}(\Omega) = F_{\Omega} \cdot \dot{M}(\Omega = 0) = F_{\Omega} \cdot \dot{M}_{\text{rad}}$$

$$\text{with} \quad F_{\Omega} = \frac{(1-\Gamma)^{\frac{1}{\alpha}-1}}{\left[1-\frac{\Omega^2}{2\pi G\rho_{\rm m}}-\Gamma\right]^{\frac{1}{\alpha}-1}} \tag{5}$$

where $\Gamma = L/L_{\rm Edd} = \kappa L/(4\pi cGM)$ is the Eddington factor (with κ the total opacity) and α the $T_{\rm eff}$–dependent force multiplier parameter. Enhancement factors (F_{Ω}) are generally close to one, but they may become very large when $\Gamma \gtrsim 0.7$ or $\Omega/\Omega_{\rm crit} > 0.9$ (see Georgy et al. 2011; Maeder and Meynet 2000, for more details). If critical rotation, where the centrifugal force balances gravity at the equator, is reached, mechanical mass loss may occur and produce a decretion disk (see Krtička et al. 2011, for more details). In most stellar evolution codes, the mass loss is artificially enhanced when $\Omega/\Omega_{\rm crit} \gtrsim 0.95$ to ensure that the ratio does not become larger than unity, but multidimensional simulations are required to provide new prescriptions to use in stellar evolution codes.

(3) **Rotation-driven instabilities**: The main rotation-driven instabilities are horizontal turbulence, meridional circulation, and dynamical and secular shear (see Maeder 2009, for a comprehensive description of rotation-induced instabilities).

Horizontal turbulence corresponds to turbulence along the isobars. If this turbulence is strong, rotation is constant on isobars, and the situation is usually referred to as "shellular rotation" (Zahn 1992). The horizontal turbulence is expected to be stronger than the vertical turbulence because there is no restoring buoyancy force along isobars (see Maeder 2003, for a discussion on this topic).

Meridional circulation, also referred to as Eddington–Sweet circulation, arises from the local breakdown of radiative equilibrium in rotating stars. This is due to the fact that surfaces of constant temperature do not coincide with surfaces of constant pressure. Indeed, since rotation elongates isobars at the equator, the temperature on the same isobar is lower at the equator than at the pole. This induces large-scale circulation of matter, in which matter usually rises at the pole and descends at the equator (see Fig. 1).

In this situation, angular momentum is transported inward. It is however also possible for the circulation to go in the reverse direction, and, in this second case, angular momentum is transported outward. Circulation corresponds to an advective process, which is different from diffusion because the latter can only erode gradients. Advection can either build or erode angular velocity gradients (see Maeder and Zahn 1998, for more details).

Dynamical shear occurs when the excess energy contained in differentially rotating layers is larger than the work that needs to be done to overcome the buoyancy force. The criterion for stability against dynamical shear instability is the Richardson criterion:

$$Ri = \frac{N^2}{(\partial U/\partial z)^2} > \frac{1}{4} = Ri_c, \tag{6}$$

where U is the horizontal velocity, z the vertical coordinate, and N^2 the Brunt–Väisälä frequency.

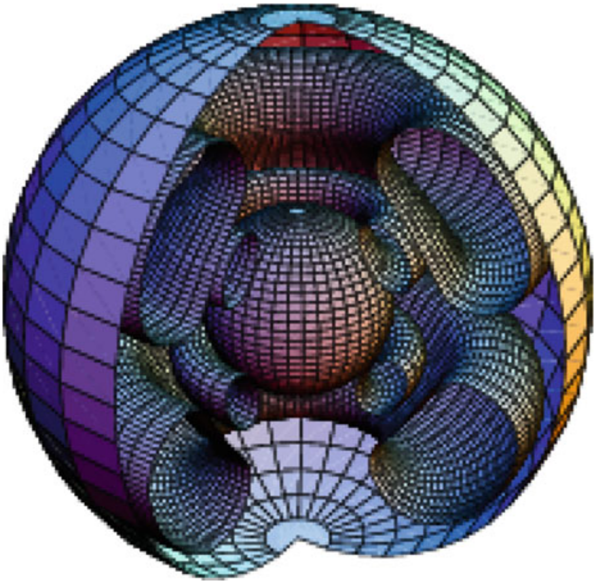

Fig. 1 Streamlines of meridional circulation in a rotating 20 $M_\odot$ model with solar metallicity and $v_{\rm ini} = 300\,{\rm km\,s^{-1}}$ at the beginning of the H–burning phase. The streamlines are in the meridian plane. In the upper hemisphere on the right section, matter is turning counterclockwise along the outer streamline and clockwise along the inner one. The outer sphere is the star surface and has a radius equal to 5.2 $R_\odot$. The inner sphere is the outer boundary of the convective core. It has a radius of 1.7 $R_\odot$ (Illustration taken from Meynet and Maeder 2002a)

The critical value of the Richardson criterion, $Ri_c = 1/4$, corresponds to the situation where the excess kinetic energy contained in the differentially rotating layers is equal to the work done against the restoring force of the density gradient (also called buoyancy force). It is therefore used by most authors as the limit for the occurrence of the dynamical shear. Studies by Canuto (2002) show that turbulence may occur as long as $Ri \lesssim Ri_c \sim 1$. This critical value is consistent with numerical simulations done by Brüggen and Hillebrandt (2001) where they find shear mixing for values of Ri greater than 1/4 (up to about 1.5). The latest 3D hydrodynamic simulations (Edelmann et al. 2017), however, confirm the theoretical value of 1/4 and that this instability is reasonably implemented in 1D models although the physical extent of the instability needs to revised.

Different dynamical shear diffusion coefficients, D, can be found in the literature. The one used in GENEC is:

$$D = \frac{1}{3} v l = \frac{1}{3}\,\frac{v}{l}\,l^2 = \frac{1}{3}\,r\frac{{\rm d}\Omega}{{\rm d}r}\,\Delta r^2 = \frac{1}{3}\,r\Delta\Omega\,\Delta r \tag{7}$$

where r is the mean radius of the zone where the instability occurs, $\Delta\Omega$ is the variation of Ω over this zone, and Δr is the extent of the zone. The zone is the reunion of consecutive shells where $Ri < Ri_c$ (see Hirschi et al. 2004, for more details and references).

If the differential rotation is not strong enough to induce dynamical shear, it can still induce the secular shear instability when thermal turbulence reduces the effect of the buoyancy force. The secular shear instability occurs therefore on the thermal time scale, which is much longer than the dynamical one. Note that the way the inhibiting effect of the molecular weight (μ) gradients on secular shear is taken into account impacts strongly the efficiency of the shear. In some work, the inhibiting effect of μ gradients is so strong that secular shear is suppressed below a certain threshold value of differential rotation (Heger et al. 2000). In other work (Maeder 1997), thermal instabilities and horizontal turbulence reduce the inhibiting effect of the μ gradients. As a result, shear is not suppressed below a threshold value of differential rotation but only decreased when μ gradients are present.

There are other minor instabilities induced by rotation: the GSF instability (Fricke 1968; Goldreich and Schubert 1967; Hirschi and Maeder 2010), the ABCD instability (Heger et al. 2000; Knobloch and Spruit 1983), and the Solberg–Høiland instability (Kippenhahn and Weigert 1990). The GSF instability is induced by axisymmetric perturbations. The ABCD instability is a kind of horizontal convection. Finally, Solberg–Høiland stability criterion is the criterion that should be used instead of the Ledoux or Schwarzschild criterion in rotating stars. However, including the dynamical shear instability also takes into account the Solberg–Høiland instability (Hirschi et al. 2004).

2.3.1 Transport of Angular Momentum

For shellular rotation, the equation of transport of angular momentum (Zahn 1992) in the vertical direction is (in Lagrangian coordinates):

$$\rho \frac{d}{dt}\left(r^2 \Omega\right)_{M_r} = \frac{1}{5r^2}\frac{\partial}{\partial r}\left(\rho r^4 \Omega U(r)\right) + \frac{1}{r^2}\frac{\partial}{\partial r}\left(\rho D r^4 \frac{\partial \Omega}{\partial r}\right) , \tag{8}$$

where $\Omega(r)$ is the mean angular velocity at level r, $U(r)$ the vertical component of the meridional circulation velocity, and D the diffusion coefficient due to the sum of the various turbulent diffusion processes (convection, shears, and other rotation-induced instabilities apart from meridional circulation). Note that angular momentum is conserved in the case of contraction or expansion. The first term on the right hand side, corresponding to meridional circulation, is an *advective* term. The second term on the right hand side, which corresponds to the diffusion processes, is a *diffusive* term. The correct treatment of advection is very costly numerically because Eq. 8 is a fourth-order equation (the expression of $U(r)$ contains third-order derivatives of Ω; see Zahn 1992). This is why some research groups treat meridional circulation in a diffusive way (see, e.g., Heger et al. 2000) with the risk of transporting angular momentum in the wrong direction (in the case meridional circulation builds gradients).

2.3.2 Transport of Chemical Species

The transport of chemical elements is also governed by a diffusion–advection equation like Eq. 8. However, if the horizontal component of the turbulent diffusion is large, the vertical advection of the elements (but not that of the angular momentum) can be treated as a simple diffusion (Chaboyer and Zahn 1992) with a diffusion coefficient $D_{\rm eff}$,

$$D_{\rm eff} = \frac{\mid rU(r) \mid^2}{30 D_h} , \tag{9}$$

where D_h is the coefficient of horizontal turbulence (Zahn 1992). Equation 9 expresses that the vertical advection of chemical elements is severely inhibited by the strong horizontal turbulence characterized by D_h. The change of the mass fraction X_i of the chemical species i is simply

$$\left(\frac{dX_i}{dt}\right)_{M_r} = \left(\frac{\partial}{\partial M_r}\right)_t \left[(4\pi r^2\rho)^2 D_{\text{mix}} \left(\frac{\partial X_i}{\partial M_r}\right)_t\right] + \left(\frac{dX_i}{dt}\right)_{\text{nuclear}}, \tag{10}$$

where the second term on the right accounts for composition changes due to nuclear reactions. The coefficient D_{mix} is the sum $D_{\text{mix}} = D + D_{\text{eff}}$, where D is the term appearing in Eq. 8 and D_{eff} accounts for the combined effect of advection and horizontal turbulence.

2.3.3 Interaction Between Rotation and Magnetic Fields

Circular spectro-polarimetric surveys have obtained evidence for the presence of magnetic fields at the surface of OB stars (see, e.g., the review by Walder et al. 2011, and references therein). The origin of these magnetic fields is still unknown. It might be fossil fields or fields produced through a dynamo mechanism.

The central question for the evolution of massive stars is whether a dynamo is at work in internal radiative zones. This could have far reaching consequences concerning the mixing of the elements and the loss of angular momentum. In particular, the interaction between rotation and magnetic fields in the stellar interior strongly affects the angular momentum retained in the core and thus the initial rotation rate of pulsars and which massive stars could die as long and soft gamma-ray bursts (GRBs) see Vink et al. (2011) and the discussion in Sect. 6 in Georgy et al. (2012, and references therein).

The interplay between rotation and magnetic field has been studied in stellar evolution calculations using the Tayler–Spruit dynamo (Maeder and Meynet 2005; Spruit 2002). Some numerical simulations confirm the existence of a magnetic instability; however the existence of the dynamo is still debated (Braithwaite 2006; Zahn et al. 2007).

The Tayler–Spruit dynamo is based on the fact that a purely toroidal field $B_\varphi(r, \vartheta)$, even very weak, in a stably stratified star is unstable on an Alfvén time scale $1/\omega_{\text{A}}$. This is the first magnetic instability to appear. It is non-axisymmetric of type $m = 1$ (Spruit 2002), occurs under a wide range of conditions, and is characterized by a low threshold and a short growth time. In a rotating star, the instability is also present; however the growth rate σ_{B} of the instability is, if $\omega_{\text{A}} \ll \Omega$,

$$\sigma_{\text{B}} = \frac{\omega_{\text{A}}^2}{\Omega}, \tag{11}$$

instead of the Alfvén frequency ω_{A}, because the growth rate of the instability is reduced by the Coriolis force (Spruit 2002). One usually has the following ordering of the different frequencies, $N \gg \Omega \gg \omega_{\text{A}}$. In the sun, one has $N \approx 10^{-3}\ \text{s}^{-1}$,

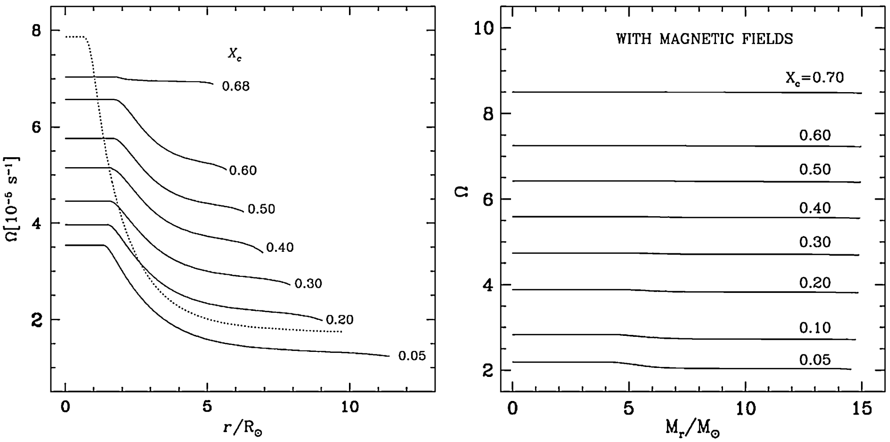

Fig. 2 *Left*: evolution of the angular velocity Ω as a function of the distance to the center in a 20 $M_\odot$ star with v_{ini} = 300 km s^{-1}. X_c is the hydrogen mass fraction at the center. The *dotted line* shows the profile when the He–core contracts at the end of the H-burning phase. *Right*: rotation profiles at various stages of evolution (labelled by the central H content X_c) of a 15 $M_\odot$ model with $X = 0.705$, $Z = 0.02$, an initial velocity of 300 km s^{-1} and magnetic field from the Tayler–Spruit dynamo (Taken from Maeder and Meynet 2005)

$\Omega = 3 \times 10^{-6}$ s^{-1}, and a field of 1 kG would give an Alfvén frequency as low as $\omega_A = 4 \times 10^{-9}$ s^{-1} (where N is the Brunt–Väisälä frequency).

This theory enables us to establish the two quantities that we are mainly interested in for stellar evolution: the magnetic viscosity ν, which expresses the mechanical coupling due to the magnetic field **B**, and the magnetic diffusivity η, which expresses the transport by a magnetic instability and thus also the damping of the instability. The parameter η also expresses the vertical transport of the chemical elements and enters Eq. 10, while the viscosity ν determines the vertical transport of the angular momentum by the magnetic field and enters the second term on the right-hand side of Eq. 8.

Figure 2 shows the differences in the internal Ω–profiles during the evolution of a 20 $M_\odot$ star with and without magnetic field created by the Tayler–Spruit dynamo. Without magnetic field, the star has a significant differential rotation, while Ω is almost constant when a magnetic field created by the dynamo is present. It is not perfectly constant, otherwise there would be no dynamo. In fact, the rotation rapidly adjusts itself to the minimum differential rotation necessary to sustain the dynamo. One could then assume that the mixing of chemical elements is suppressed by magnetic fields. This is, however, not the case since the interplay between magnetic fields and the meridional circulation tends to lead to more mixing in models including magnetic fields compared to models not including magnetic fields (Maeder and Meynet 2005). Fast-rotating models of GRB progenitors calculated by Yoon et al. (2006) also experience a strong chemical internal mixing leading to the stars undergoing quasi-chemical homogeneous evolution. The study of the interaction between rotation and magnetic fields is still under development (see, e.g., Potter et al. 2012, for a different rotation-magnetic field interaction theory, the $\alpha - \Omega$ dynamo, and its impact on massive star evolution), and the next 10 years will certainly provide new insights on this important topic.

2.3.4 Other Input Physics

The other key input physics that are essentials for the computation of stellar evolution models are nuclear reactions, mass loss prescriptions (discussed above), the equation of state, opacities, and neutrino losses. Stellar evolution codes are now able to include larger and more flexible nuclear reaction network (see, e. g., Frischknecht et al. 2010, for a description of the implementation of a flexible network in GENEC). Nuclear physics and other inputs are described for other codes, for example, in Paxton et al. (2011) and Chieffi et al. (1998).

3 Evolution of Massive Stars and Key Abundances

In this section, we review the general evolution of massive stars at solar metallicity. The models and plots presented in this chapter are taken from Hirschi et al. (2004) unless otherwise stated. In that study, stellar models of 12, 15, 20, 25, 40, and 60 $M_{\odot}$ at solar metallicity, with initial rotational velocities of 0 and 300 $\mathrm{km\,s^{-1}}$, respectively, were computed, thus covering most of the massive star range. Other recent grids of models at solar metallicity can be found in Ekström et al. (2012), Chieffi and Limongi (2013), and Sukhbold and Woosley (2014). Models for lower-mass and higher-mass massive stars can be found in, e.g., Jones et al. (2013) and Yusof et al. (2013), respectively.

3.1 Evolution of Surface Properties (HR Diagram) and Lifetimes

For many aspects discussed in this chapter, we will focus on the 20 $M_{\odot}$ non-rotating and rotating models. Figure 3 (*left*) shows the evolutionary tracks of different 20 $M_{\odot}$ models in the HR diagram and thus how the surface properties of these stars evolve. The non-rotating model is representative of the lower end of massive stars, which keep an extended hydrogen-rich envelope, end as red supergiant, and produce type II supernovae. The 300 $\mathrm{km\,s^{-1}}$ model is representative of the higher end of massive stars, for which most or all of the H-rich envelope is lost via stellar winds and the star ends as a hot star, generally a Wolf–Rayet star and produce a type Ib or Ic supernova depending on how much helium is left. These two models also show the impact of rotation on the evolution of massive stars. The additional models with intermediate rotation (v_{ini}= 100 and 200 $\mathrm{km\,s^{-1}}$) show the smooth transition from non-rotating to fast-rotating models. HR diagrams covering the full IMF can be found in Ekström et al. (2012).

As mentioned in the Introduction, massive stars go through six burning stages: H, He, C, Ne, O, and Si burning. The lifetimes of these stages are plotted in Fig. 3

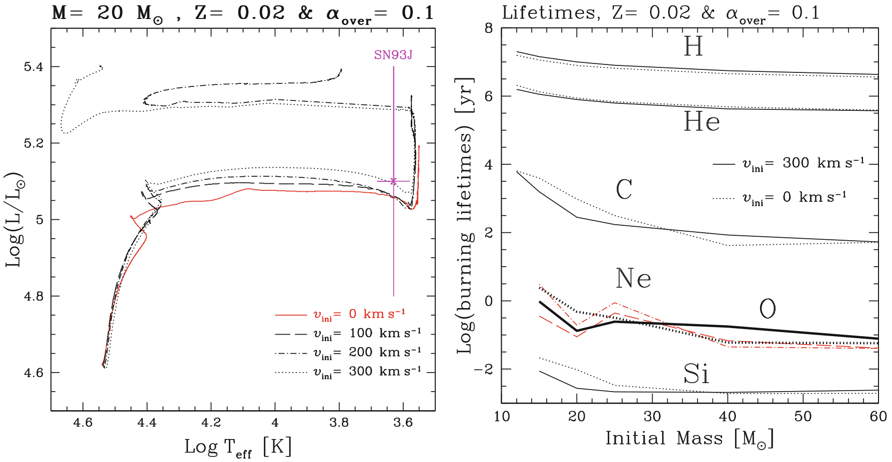

Fig. 3 *Left*: HR diagram for 20 $M_\odot$ models: *solid, dashed, dotted–dashed, and dotted lines* correspond, respectively, to v_{ini}= 0, 100, 200, and 300 km s^{-1}. We also indicate the position of the progenitor of SN 1993J. *Right*: Burning lifetimes as a function of the initial mass and velocity. *Solid and dotted lines* correspond, respectively, to rotating and non-rotating models. *Long dashed* and *dotted–dashed lines* are used for rotating and non-rotating Ne-burning lifetimes to point out that they are to be considered as estimates (See text)

(*right*). Whereas H- and He-burning stages last for roughly 10^{6-7} and 10^{5-6} years, respectively, the lifetimes for the advanced phases is much shorter. This is due to neutrino losses dominating energy losses over radiation from C burning onward. C-, Ne-, O-, and Si-burning phases last about 10^{2-3}, 1, 1, and 10^{-2} years, respectively. Concerning the effects of rotation and mass loss, there is a mass range where rotational mixing ($M \lesssim 30 M_\odot$) or mass loss ($M \gtrsim 30 M_\odot$) dominates over the other process. For $M \lesssim 30 M_\odot$, rotation-induced mixing extends the H-burning lifetime and as a consequence shortens slightly He-burning lifetimes. For the advanced phases, rotation makes star behave like more massive stars. This is clearly seen for C-burning lifetimes, which are shorter for rotating models. For $M \gtrsim 30 M_\odot$, strong mass loss leads to degeneracy in the lifetime and final properties.

3.2 Evolution of Central Properties in the Log T_c–Log ρ_c Diagram

Figure 4 (left) shows the tracks of the 15 and 60 $M_\odot$ models throughout their evolution in the central temperature versus central density plane (Log T_c–Log ρ_c diagram). Figure 4 (right) zooms in the advanced stages of the 12, 20, and 40 $M_\odot$ models. It is also very instructive to look at Kippenhahn diagrams (Fig. 8) in order to follow the evolution of the structure. We again identify two categories of stellar models: those for which the evolution is mainly affected by mass loss (with an inferior mass limit of about 30 $M_\odot$) and those for which the evolution is mainly

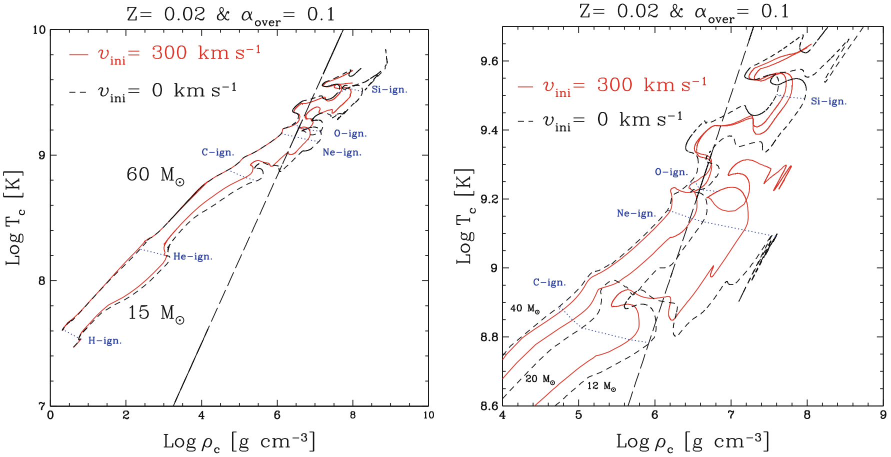

Fig. 4 Log T_c vs Log ρ_c diagrams. *Left*: evolutionary tracks for the 15 and 60 $M_\odot$ models. *Right*: evolutionary tracks zoomed in the advanced stages for the 12, 20, and 40 $M_\odot$ models. *Solid lines* are rotating models and *dashed lines* are nonrotating models. The ignition points of every burning stage are connected with *dotted lines*. The additional *long dashed line* corresponds to the limit between nondegenerate and degenerate electron gas ($P^{\text{el}}_{\text{perfect gas}} = P^{\text{el}}_{\text{degenerate gas}}$)

affected by rotational mixing (already identified in Sect. 3.1). We can see that for the 12, 15, and 20 $M_\odot$ models, the rotating tracks have a higher temperature and lower density due to more massive convective cores. The bigger cores are due to the effect of mixing, which largely dominates the structural effects of the centrifugal force. On the other hand, for the 40 and 60 $M_\odot$ models, mass loss dominates mixing effects, and the rotating model tracks in the Log T_c–Log ρ_c plane are at the same level or below the non-rotating ones.

In order to understand the evolutionary tracks in the Log T_c–Log ρ_c plane, we need to look at the different sources of energy at play. These are the nuclear energy, the neutrino and photon energy losses, and the gravitational energy (linked to contraction and expansion). The different energy production rates at the star center are plotted in Fig. 5 as a function of the time left until core collapse. Going from the left to the right in Fig. 5, the evolution starts with H burning where ε_H dominates. In response, a small expansion occurs (ε_g negative and very small movement to lower densities in the 15 $M_\odot$ model during H burning in Fig. 4). At the end of H burning, the star contracts non-adiabatically ($T \sim \rho^{1/3}$, every further contraction is also non-adiabatic). The contraction increases the central temperature. This happens very quickly and is seen in the sharp peak of ε_g between H- and He-burning phases. When the temperature is high enough, He burning starts, ε_{He} dominates, and contraction is stopped. Note that during the H- and He-burning phases, most of the energy is transferred by radiation on a thermal time scale. After He burning, neutrino losses ($\varepsilon_\nu < 0$) overtake photon losses. This accelerates the evolution because neutrinos escape freely. During burning stages, the nuclear energy production stops

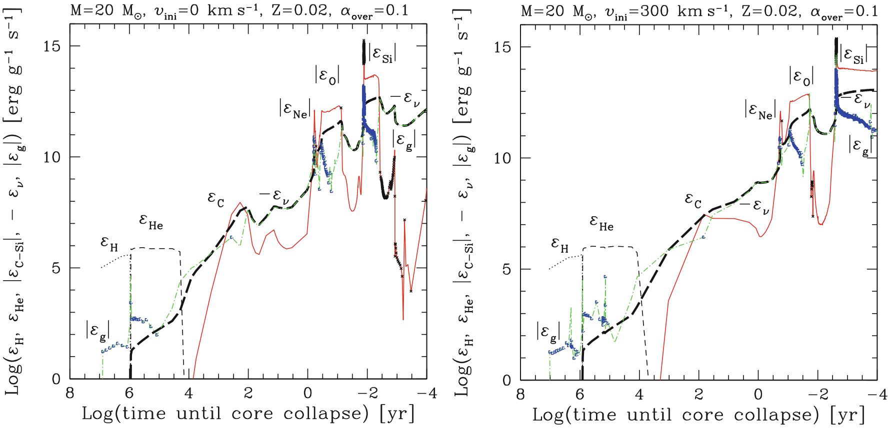

Fig. 5 Log of the energy production rate per unit mass at the star center as a function of the time left until core collapse for the nonrotating (*left*) and rotating (*right*) 20 $M_\odot$ models. Nuclear energy production rates during H and He burnings are shown in *dotted* (ε_H) and *dashed* (ε_{He}) *lines*, respectively. The *solid* line corresponds to the nuclear energy production rate in absolute value during the advanced stages (ε_C–ε_{Si}). *Black* crosses are drawn on top of the line whenever the energy production rate is negative. The thick *long dashed line* is the energy loss rates due to neutrinos multiplied by -1 ($-\varepsilon_\nu$). Finally the gravitational energy production rate in absolute value is plotted in the *dotted–dashed* line (ε_g). *Blue squares* are plotted on top when this energy is negative. Note that negative gravitational energy production corresponds to an expansion

the contraction if $\varepsilon_{nucl} \sim -\varepsilon_\nu$ (see C burning for the rotating model) or even provokes an expansion when $\varepsilon_{nucl} > -\varepsilon_\nu$ (most spectacular during Si burning). Central density decreases when the central regions expand (see Fig. 4). Once the iron core is formed, there is no more nuclear energy available, while neutrino losses are still present and the core collapses.

3.2.1 Transition Between Massive and Intermediate Stars (8–12 $M_\odot$ Stars)

Recent models for the transition between massive and intermediate stars can be found in Jones et al. (2013), Takahashi et al. (2013), and Woosley and Heger (2015), and older models can be found in Nomoto (1984, 1987) and Ritossa et al. (1999). We will base our discussion on the models presented in Jones et al. (2013) and shown in Fig. 6. Similar trends and conclusions are found in the other studies. The evolution and fate of stars in this mass range are sensitive to convective boundary mixing (CBM) treatment (e.g., overshooting), mass loss, and CO core growth. Different choices of CBM lead to the transition mass being shifted up and down, but we expect the same transitions and regimes to take place for different choices of CBM. The fate of super-AGB stars (SAGB, AGB stars that undergo carbon burning but not neon or subsequent burning stages) is highly sensitive to the mass loss prescription on the SAGB and the rate at which the core grows (Poelarends et al. 2008). Mass loss and core growth compete against each other.

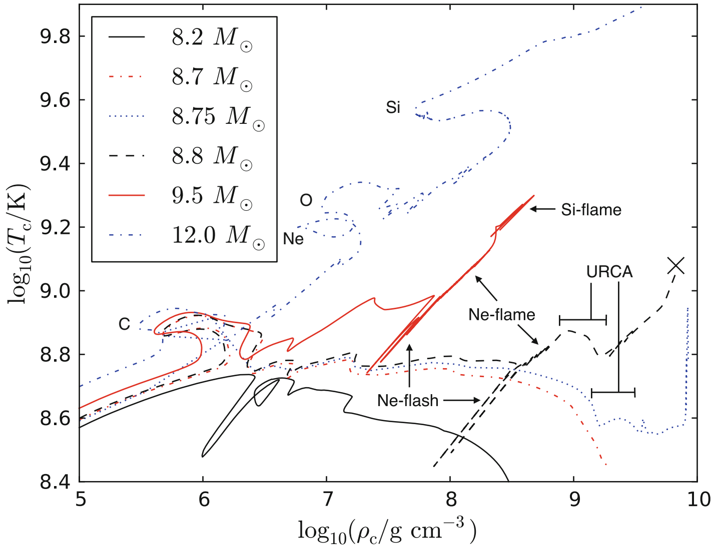

Fig. 6 The divergence of the models following C burning in the $\log_{10}(\rho_c) - \log_{10}(T_c)$ plane; the cross shows from where the evolution of the 8.8 $M_\odot$ model was continued with the AGILE-BOLTZTRAN 1D hydro-code (taken from Jones et al. 2013)

At solar metallicity, mass loss often wins, and only a very narrow mass range at the top of the SAGB mass range will end as electron-capture supernovae (ECSN). The 8.7 and 8.75 $M_\odot$ models represent models in this narrow mass range. The 8.2 $M_\odot$ model represents models in the SAGB mass range for which mass loss wins, and this model will end as a one white dwarf (WD). Previous studies (see Nomoto 1984, and references therein) show that the core mass limit for neon ignition is very close to 1.37 $M_\odot$, which recent models confirm. Indeed, in all models with initial mass greater than 8.8 $M_\odot$, a CO-core develops, with a mass that exceeds the limit for neon ignition, $M_{\rm CO}(8.8\,M_\odot,\ 9.5\,M_\odot,\ 12.0\,M_\odot) = 1.3696,\ 1.4925,\ 1.8860\,M_\odot$. A temperature inversion develops in the core following the extinction of carbon burning in both the 8.8 $M_\odot$ and 9.5 $M_\odot$ models. The neutrino emission processes that remove energy from the core are (over)compensated by heating from gravitational contraction in more massive stars. However in these lower-mass stars, the onset of partial degeneracy moderates the rate of contraction, and hence neutrino losses dominate, cooling the central region. As a result, the ignition of neon in the 8.8 and 9.5 $M_\odot$ models takes place off center. These two models then go through neon(/oxygen; oxygen also burns via fusion in this situation) flashes followed by the development of a neon(/oxygen) flame. Owing to the high densities in the cores of these stars, the products of neon and oxygen burning are more neutron rich than in more massive stars. This results in an electron fraction in the shell of as low as $Y_{\rm e} \approx 0.48$. Due to its higher degeneracy, $Y_{\rm e}$ decreases faster in the 8.8 $M_\odot$, and it contracts faster than the time needed for the neon/oxygen flame to reach the center of the star, both processes being helped by URCA pair processes. The core of the 8.8 $M_\odot$ model continuously contracts until the center reaches the critical density for electron captures by ^{24}Mg, quickly followed by further contraction to the critical density for those by ^{20}Ne (see Fig. 6), and this model results in core collapse. The 8.8 $M_\odot$ model produces a ECSNe as for the 8.75 $M_\odot$ model but via a new evolutionary path named “failed massive star” rather than via the SAGB evolutionary path. The “failed massive star” path is also expected to take place for a narrow mass range, but it does not critically depend on the uncertainties linked to mass loss, which is the case for the SAGB progenitors of ECSNe. Similarly to the 8.8 $M_\odot$ model starting neon burning off center, the 9.5 $M_\odot$ model starts silicon burning off center in a shell that later propagates toward the center. This is another example of the continuous transition toward massive stars, in which all the burning stages begin centrally. Although we have not evolved this model to its conclusion, we expect that silicon burning will migrate to the center, producing an iron core, and that it will finally collapse as an iron core-collapse SN (FeCCSN). The canonical massive star evolution (igniting C, Ne, O, and Si burning centrally) leading to FeCCSN is expected to take place for stars with masses above 10 $M_\odot$. This mass range is represented by the 12 $M_\odot$ in Fig. 6.

At the other end of the IMF, very massive stars evolve far away from degeneracy. Very massive stars may encounter instead the pair-creation instability at very high temperatures (see Yusof et al. 2013, and references therein).

3.3 Angular Velocity, Ω, and Momentum, *j*, Evolution

Figure 7 (*left*) shows the evolution of Ω inside a 25 $M_\odot$ model from the ZAMS until the end of the core Si-burning phase. The evolution of Ω results from many different processes: convection enforces solid body rotation, contraction and expansion, respectively, increases and decreases Ω in order to conserve angular momentum, shear (dynamical and secular) erodes Ω gradients, while meridional circulation may erode or build them up, and finally mass loss may remove angular momentum from the surface. If during the core H-burning phase, all these processes may be important, from the end of the MS phase onward, the evolution of Ω is mainly determined by convection, by the local conservation of the angular momentum and, during the core He-burning phase only for the most massive stars, by mass loss.

During the MS phase, Ω decreases in the whole star. When the star becomes a red supergiant (RSG), Ω at the surface decreases significantly due to the expansion of the outer layers. Note that the envelope is gradually lost by winds in the 25 $M_\odot$ model, whereas in lower mass stars, a very slowly rotating envelope remains until the pre-supernova stage. In the center, Ω significantly increases when the core contracts and then the Ω profile flattens due to convection. Ω reaches values of the order of 1 s^{-1} at the end of Si burning. It never reaches the local breakup angular velocity limit, Ω_c, although, when local conservation holds, $\Omega_r/\Omega_c \propto r^{-1/2}$.

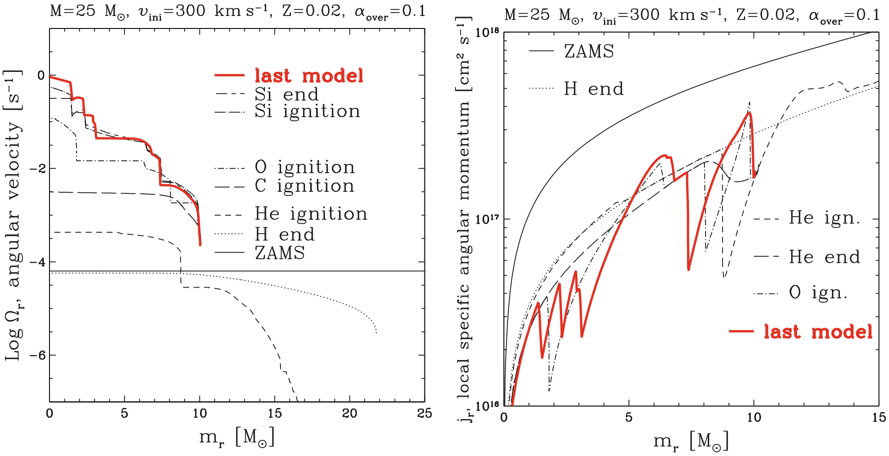

Fig. 7 Angular velocity (*left*) and local specific angular momentum (*right*) profiles as a function of the Lagrangian mass coordinate, m_r inside the 25 $M_\odot$ model (v_{ini}= 300 km s^{-1}) at various evolutionary stages

Figure 7 (*right*) shows the evolution of the specific angular momentum, $j_r = 2/3\,\Omega_r r^2$, in the central region of a 25 $M_\odot$ stellar model. The specific angular momentum remains constant under the effect of pure contraction or expansion but varies when transport mechanisms are active. One sees that the transport processes remove angular momentum from the central regions. Most of the removal occurs during the core H-burning phase. Still some decrease occurs during the core He-burning phase, and then the evolution is mostly governed by convection, which transports the angular momentum from the inner part of a convective zone to the outer part of the same convective zone. This produces the teeth seen in the figure. The angular momentum of the star at the end of Si burning is very similar to what it was at the end of He burning. More recent models including the effects of magnetic fields (see, e.g., Heger et al. 2005) lead to slower rotation at the pre-supernova stage, especially if the star goes through a red supergiant phase. These slower pre-supernova rotation rates better reproduce the observed rotation rate of pulsar. The general evolution of the angular velocity and momentum remains, however, qualitatively similar to the models above. Furthermore, some stars, especially if they remain compact throughout their evolution, may retain fast rotation in their core (Yoon et al. 2006) and lead to exotic explosions such as gamma-ray bursts.

3.4 Structure and Abundance Evolution and Pre-supernova Properties

Figure 8 shows the evolution of the structure (Kippenhahn diagram) for 20 $M_\odot$ models. The y-axis represents the mass coordinate and the x-axis the time left until core collapse. The black zones represent convective zones. The abbreviations of the

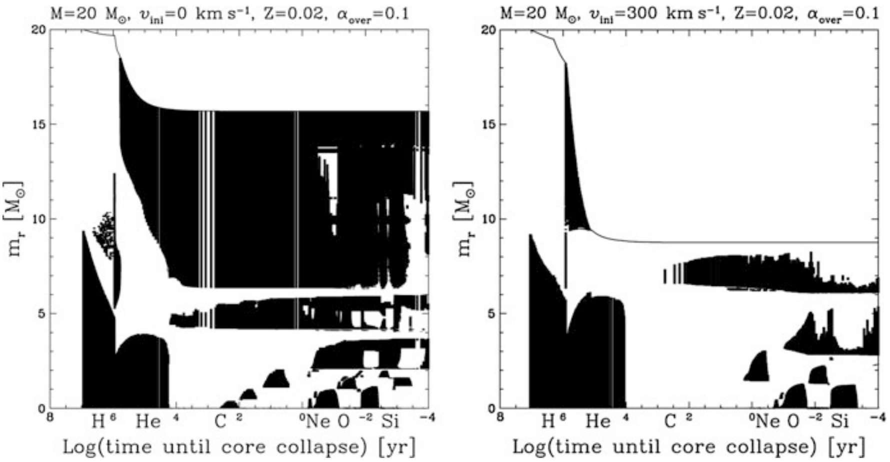

Fig. 8 Kippenhahn diagrams for the non-rotating (*left*) and v_{ini}= 300 km s^{-1} (*right*) 20 $M_\odot$ models. The *black zones* correspond to convective regions (see text). Note that these plots are produced by drawing *black vertical lines* for a subset of the time steps of the model and thus the *vertical white lines* around log(time left until collapse) $\sim$ 3 are only due to the drawing technique and the models remain convective in between neighboring *black vertical lines*

various burning stages are written below the graph at the time corresponding to the central burning stages. We note the complex succession of the different convective zones during the advanced phases. Sukhbold and Woosley (2014) study in detail the complex convective history in massive stars. In particular, their Fig. 13 shows how the location in mass of the lower boundary of carbon-burning convective shells plays a key role in determining the compactness (Ertl et al. 2016; O'Connor and Ott 2011) at the pre-supernova stage. It is worth to note that a few physical ingredients of the stellar models influence carbon burning in general and thus the exact location of the convective shells and the compactness for a given initial mass. Carbon burning is sensitive to the amount of carbon (relative to oxygen) left at the end of helium burning. This in turn is influenced by the $^{12}\mathrm{C}(\alpha,\gamma)^{16}\mathrm{O}$ rate relative to the triple-α rate (Tur et al. 2009). Convective boundary criteria and mixing prescriptions also affect the carbon left over at the end of helium burning. Using Ledoux rather than Schwarzschild generally leads to smaller helium-burning cores and more carbon leftover. Extra mixing, especially toward the end of He burning brings fresh α particles that can capture on ^{12}C and reduce its left over abundance. Finally rotation-induced mixing, as is clearly seen in Fig. 8, leads to significantly larger helium cores and less leftover carbon and leads to radiative core carbon burning (*right* panel). The other differences between non-rotating and rotating models are the following. We can see that small convective zones above the central H-burning core disappear in rotating models. Also visible is the loss of the hydrogen-rich envelope in the rotating models. The non-rotating 20 $M_\odot$ model is representative of the stars below 20 $M_\odot$, while the rotating 20 $M_\odot$ model is representative of the non-rotating and rotating models above 30 $M_{\odot}$. Above 30 $M_{\odot}$, all have very similar convective zones history after He burning, having all lost their H-rich envelope and all undergoing core C burning under radiative conditions. The main difference between stars above 30 $M_{\odot}$ and the rotating 20 $M_{\odot}$ model is that stars above 30 $M_{\odot}$ have one large carbon convective shell that sits around 3 $M_{\odot}$ and thus does not influence much the final stages and the compactness at the pre-supernova stages. The complex history of convective zones and the uncertainties in the input physics mentioned here make it very hard to predict the exact explosion properties of a star of a given initial mass. Nevertheless, it is likely, as in the case of SAGB stars, that the same transitions would occur (e.g., from convective to radiative core carbon burning) even if the input physics changes. Convective boundary mixing during carbon burning (and other stages), if able to change the extent of convective burning shells, might affect the compactness of supernova progenitor significantly. 3D hydrodynamic simulations of convective boundary mixing (see, e.g., Cristini et al. 2017) will hopefully help constrain the 1D prescriptions used in stellar evolution codes, in the near future (Arnett et al. 2015).

3.5 Abundances Evolution

Figures 9 and 10 show the evolution of the abundances of the main isotopes inside the non-rotating (*left*) and rotating (*right*) 20 $M_{\odot}$ models at the end of each central burning episode. As hydrogen burns via the CNO and ^{14}N(p,γ) is the slowest reaction in the cycle, most of the ^{12}C and ^{16}O is transformed into N in the convective core. At the end of H burning, we notice the smoother profiles in the rotating model, consequence of the rotational mixing. During He burning, triple-α and (α,γ) reactions produce mostly ^{12}C and ^{16}O with traces of heavier multiple α-elements ^{20}Ne and ^{24}Mg. Double α-captures on ^{14}N leads to a significant production of ^{22}Ne. Toward the end of He burning, ^{22}Ne undergoes both (α,γ) and (α,n). This last reaction is the neutron source for the weak s-process discussed in Sect. 6. At the end of He burning, we can see that rotating models have larger core sizes and a lower total mass due to extra mixing and mass loss, respectively. We also notice the lower C/O ratio for rotating models mentioned above. The main burning products of carbon burning are ^{20}Ne, ^{23}Na (not shown here), and ^{24}Mg. The main products of Ne burning are ^{16}O, ^{23}Na, and ^{24}Mg. The main products of O burning are elements around ^{28}Si and ^{32}S. At the end of O burning, we can see that the rotating model produces much more oxygen compared to the non-rotating model (by about a factor of two). At the end of Si burning, the iron (represented by ^{56}Ni) and Si cores are slightly bigger in the rotating model. The yields of oxygen increase significantly with rotation as discussed below.

Comparing Figs. 11 and 10 shows that even though the 60 $M_{\odot}$ model has a larger CO core (between about 3 and 11 $M_{\odot}$), its inner and outer structure is quite similar to that of the rotating 20 $M_{\odot}$ star. This is due to mass loss pealing 3/4 of the initial mass of the star before the end of He burning for the 60 $M_{\odot}$ model. This means that stars with $M > 30\,M_{\odot}$ have a significant stellar wind contributions as we shall see below.

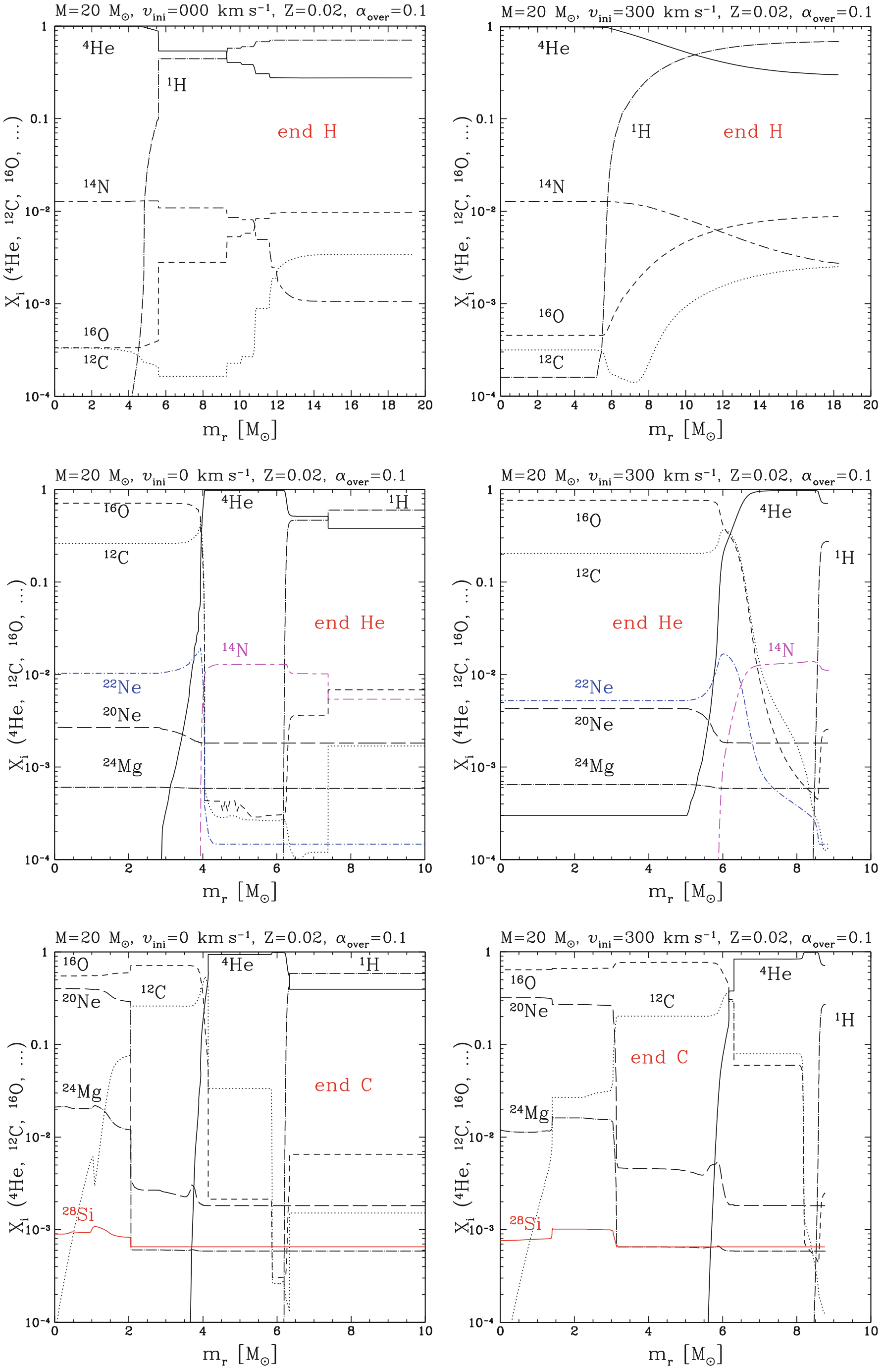

Fig. 9 Variation of the abundances in mass fraction as a function of the Lagrangian mass at the end of central hydrogen (*top*), helium (*middle*), and carbon (*bottom*) burnings for the nonrotating (*left*) and rotating (*right*) $20 M_\odot$ models

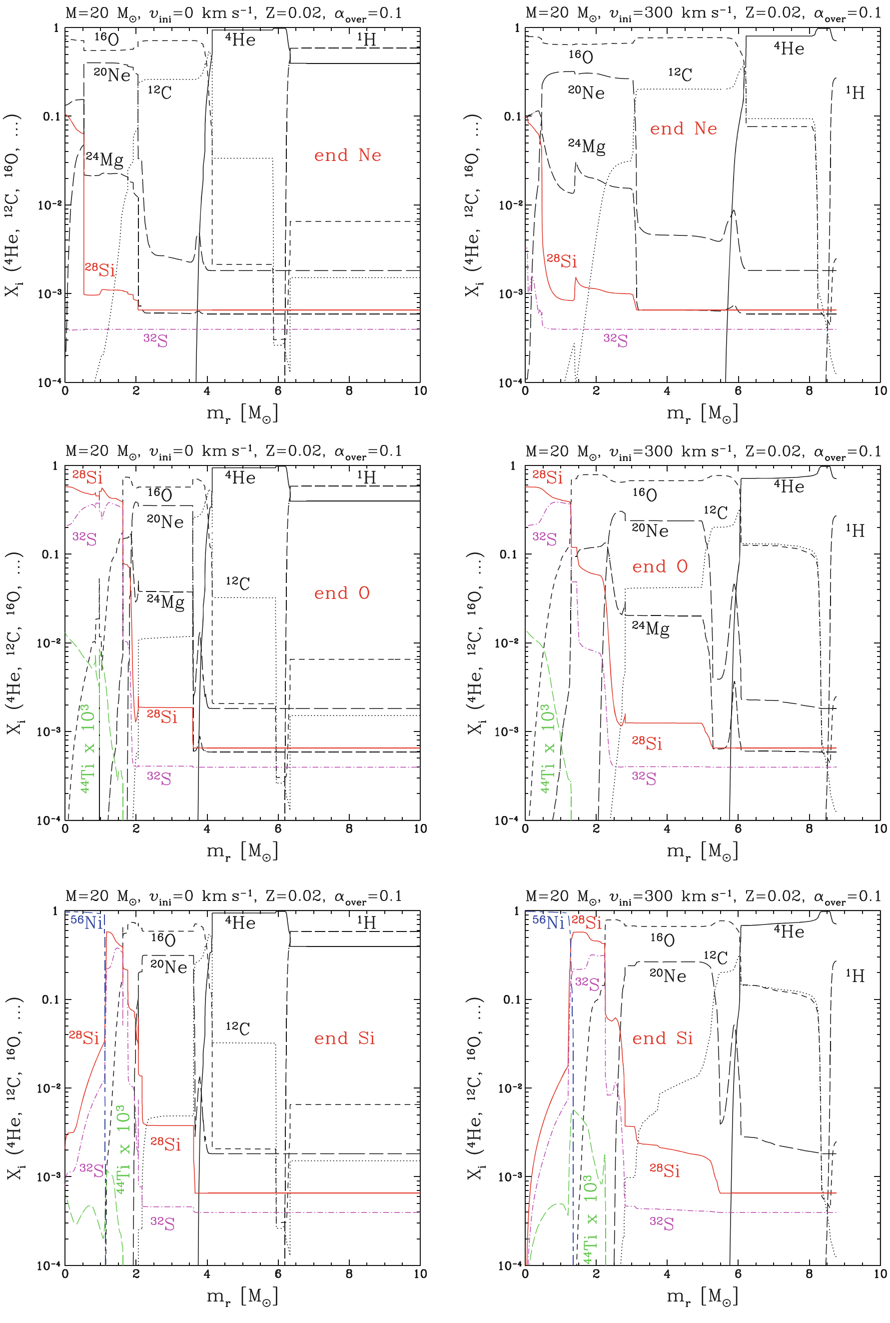

Fig. 10 Variation of the abundances in mass fraction as a function of the Lagrangian mass at the end of central neon (*top*), oxygen (*middle*), and silicon (*bottom*) burnings for the nonrotating (*left*) and rotating (*right*) $20M_\odot$ models. Note that the abundance of ^{44}Ti (*dotted–long dashed line*) is enhanced by a factor 1000 for display purposes

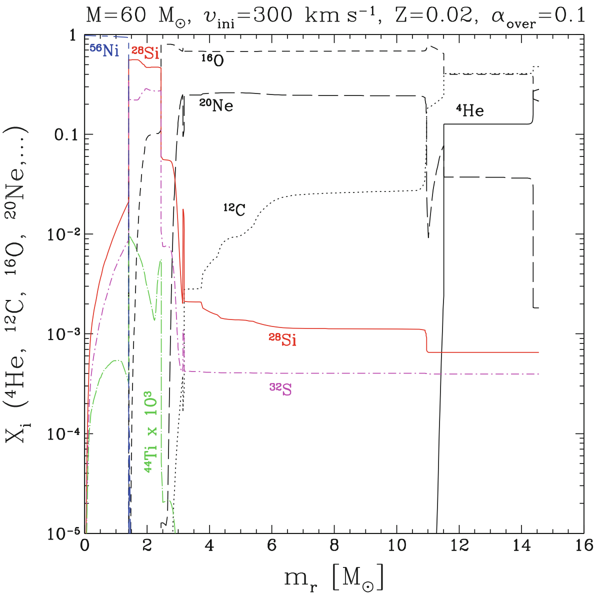

Fig. 11 Variations of the abundance (in mass fraction) as a function of the Lagrangian mass coordinate, m_r, at the end of central Si burning for the rotating 60 $M_\odot$. Note that the ^{44}Ti abundance (*dotted–long dashed line*) is enhanced by a factor 1000 for display purposes

3.6 Pre–supernova Properties

Figure 12 shows the core masses as a function of initial mass for non-rotating (dotted lines) and rotating (solid lines) models. Since rotation increases mass loss, the final mass, $M_{\rm final}$, of rotating models is always smaller than that of nonrotating ones. Note that for very massive stars ($M \gtrsim 60 M_\odot$), mass loss during the WR phase is proportional to the actual mass of the star. This produces a convergence of the final masses (see, for instance, Meynet and Maeder 2005). We can again see a general difference between the effects of rotation below and above 30 $M_\odot$. For $M \lesssim 30\,M_\odot$, rotation significantly increases the core masses due to mixing. For $M \gtrsim 30\,M_\odot$, rotation makes the star enter the WR phase at an earlier stage. The rotating star spends therefore a longer time in this phase characterized by heavy mass loss rates. This results in smaller cores at the pre-supernova stage. We can see on Fig. 12 that the difference between rotating and nonrotating models is the largest between 15 and 25 $M_\odot$. As explained above, this will have an impact on the compactness in this sensitive mass range. Improvements in input physics may reconcile model predictions with observationally determined masses of type II supernova, with a maximum below 20 $M_\odot$, named the RSG problem by Smartt (2009) if the mass range of high compactness ends up covering the mass range between about 17 and 22 $M_\odot$, while more massive stars explode as type Ib or Ic supernova or fail to explode.

Fig. 12 Core masses as a function of the initial mass and velocity at the end of core Si burning

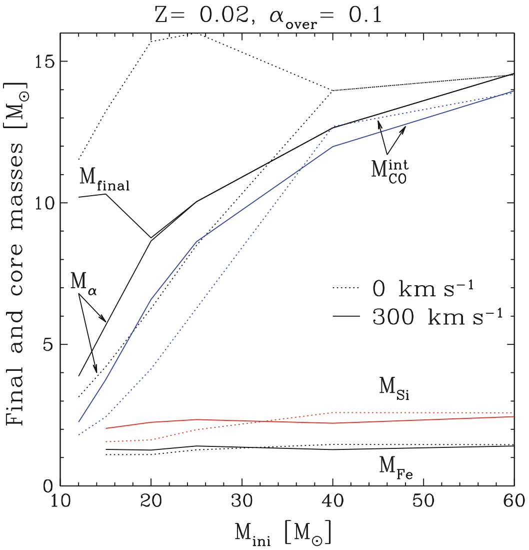

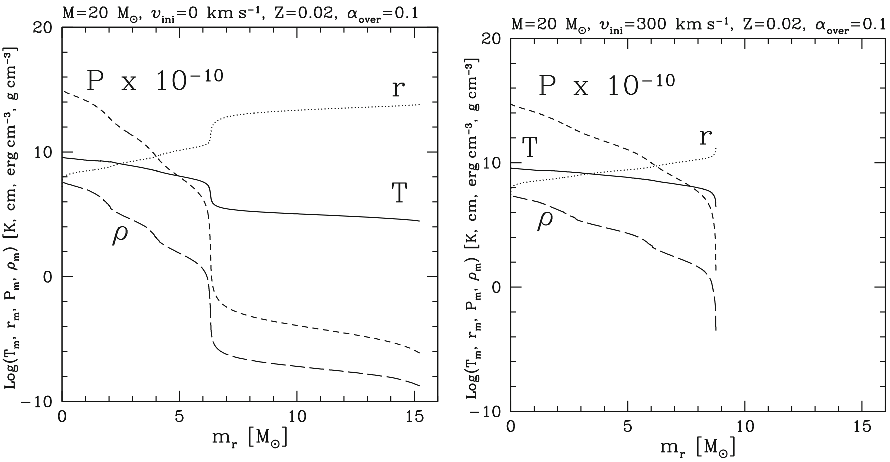

Fig. 13 Profiles of the radius, r; density, ρ; temperature, T; and pressure P at the end of core Si burning for the nonrotating (*left*) and rotating (*right*) 20 $M_\odot$ models. The pressure has been divided by 10^{10} to fit it in the diagram

As well as the chemical composition (abundance profiles and core masses) of the pre-supernova star, other parameters, like the density profile, the neutron excess (not followed in our calculations), the entropy, and the total radius of the star, play an important role in the supernova explosion. Figure 13 shows the density, temperature, radius, and pressure variations as a function of the Lagrangian mass coordinate at the end of the core Si-burning phase. Since the rotating star has lost its envelope, this truly affects the parameters toward the surface of the star. The radius of the star (BSG) is about 1% that of the nonrotating star (RSG). As said above, this modifies strongly the supernova explosion. We also see that temperature, density, and pressure profiles are flatter in the interior of rotating models due to the bigger core sizes.

4 Stellar Wind Contribution to Galactic Chemical Enrichment

Before reviewing the contribution of stellar wind to nucleosynthesis, it is useful to summarize the dependence on the initial mass of mass loss and various core masses:

Mass loss: Is very small for stars less massive than 20 $M_\odot$. It then quickly increases and becomes the dominant physical process for non-rotating stars more massive than 40 $M_\odot$. Rotation reduces the mass at which mass loss dominates to less than 30 $M_\odot$. Mass loss takes place mostly during H- and He-burning phases so stellar wind can only enrich the ISM with H- and He-burning products (elements up to silicon)

M_{final}: Due to the strong mass loss experienced by massive stars, there is no simple relation between the final mass and the initial one. The important point is that a final mass between 10 and 15 $M_\odot$ can correspond to any star with an initial mass above 15 $M_\odot$.

M_α: The core masses increase significantly with the initial mass. For very massive stars, these core masses are limited by the very important mass loss undergone by these stars: typically M_α is equal to the final mass for $M \gtrsim 20\ M_\odot$ for rotating models and for $M \gtrsim 40\ M_\odot$ for the non-rotating ones.

M_{CO}: The mass of the carbon–oxygen core is also limited by mass loss for $M \gtrsim 40\ M_\odot$ for both rotating and non-rotating models.

What is the relative importance of the wind and pre-SN contributions? Figure 14 displays the total stellar yields divided by the initial mass of the star, p_{im}^{tot}, as a function of its initial mass, m, for the non-rotating (left) and rotating (right) models. The total stellar yields, $mp_{im}^{\text{tot}} = mp_{im}^{\text{pre-SN}} + mp_{im}^{\text{wind}}$ (to be used for chemical evolution models using Eq. 2 from Maeder 1992), plotted in this figure are given in Tables 6 and 7 in Hirschi et al. (2005). The different shaded areas correspond from top to bottom to p_{im}^{tot} for ^{4}He, ^{12}C, ^{16}O, and the rest of the heavy elements. The fraction of the star locked in the remnant and the expected explosion type are shown at the bottom. The dotted areas show the wind contribution for ^{4}He, ^{12}C, and ^{16}O.

For ^{4}He, and for other H-burning products like ^{14}N and ^{26}Al, the wind contribution increases with mass and dominates for $M \gtrsim 22 M_\odot$ for rotating stars and $M \gtrsim 35 M_\odot$ for non-rotating stars, i.e., for stars which enter the WR stage. For very massive stars, the (pre-)SN contribution is negative, and this is why the dotted area is higher than the purple area for ^{4}He. In order to eject He-burning products, a star must not only become a WR star but must also become a WC star. Therefore for ^{12}C, the wind contributions only start to be significant above the following approximative mass limits: 30 and 45 $M_\odot$ for rotating and non-rotating models,

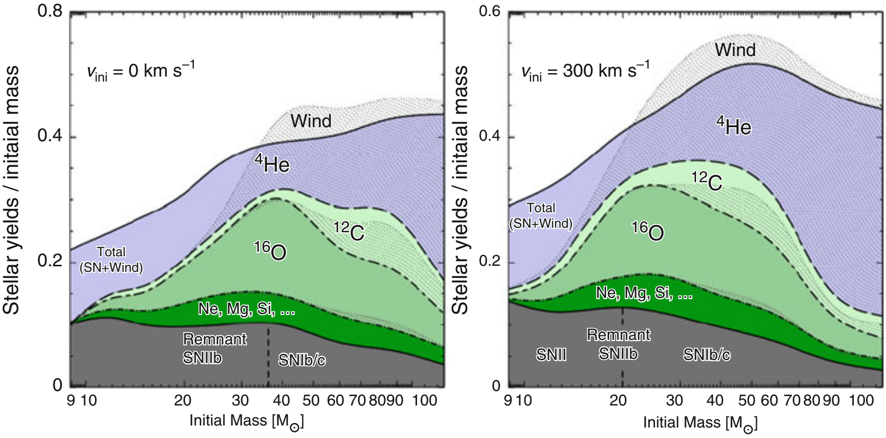

Fig. 14 Stellar yields divided by the initial mass, $p_{im}^{\rm tot}$, as a function of the initial mass for the nonrotating (*left*) and rotating (*right*) models at solar metallicity. The different total yields (divided by m) are shown as piled up on top of each other and are not overlapping. ^{4}He yields are delimited by the *top solid* and *long dashed lines* (*top shaded area*), ^{12}C yields by the *long dashed* and *short–long dashed lines*, ^{16}O yields by the *short–long dashed* and *dotted–dashed lines*, and the rest of metals by the *dotted–dashed* and *bottom solid lines*. The *bottom solid line* also represents the mass of the remnant ($M_{\rm rem}^{\rm int}/m$). The corresponding SN explosion type is also given. The wind contributions are superimposed on these total yields for the same elements between their bottom limit and the dotted line above it. Dotted areas help quantify the fraction of the total yields due to winds. Note that for ^{4}He, the total yields are smaller than the wind yields due to negative SN yields (see text). Preliminary results for masses equal to 9, 85, and 120 $M_\odot$ were used in this diagram (See Hirschi 2004)

respectively. Above these mass limits, the contribution from the wind and the pre-SN are of similar importance for carbon. Since at solar metallicity, no WO star are expected (Meynet and Maeder 2005), for ^{16}O, as for heavier elements (expect for elements produced during H burning like ^{26}Al), the wind contribution remains very small.

4.1 Comparison Between Rotating and Non-rotating Models and Convolution with the IMF

For H-burning products, the yields of the rotating models are usually higher than those of nonrotating models. This is due to larger cores and larger mass loss. Nevertheless, between about 15 and 25 $M_\odot$, the rotating yields are smaller. This is due to the fact that the winds do not expel many H-burning products yet and more of these products are burnt later in the pre-supernova evolution (giving negative SN yields). Above $40 M_\odot$, rotation clearly increases the yields of ^{4}He.

Concerning He-burning products, below 30 $M_\odot$, most of the ^{12}C comes for the pre-SN contribution. In this mass range, rotating models having larger cores also have larger yields (factor 1.5–2.5). We notice a similar dependence on the initial

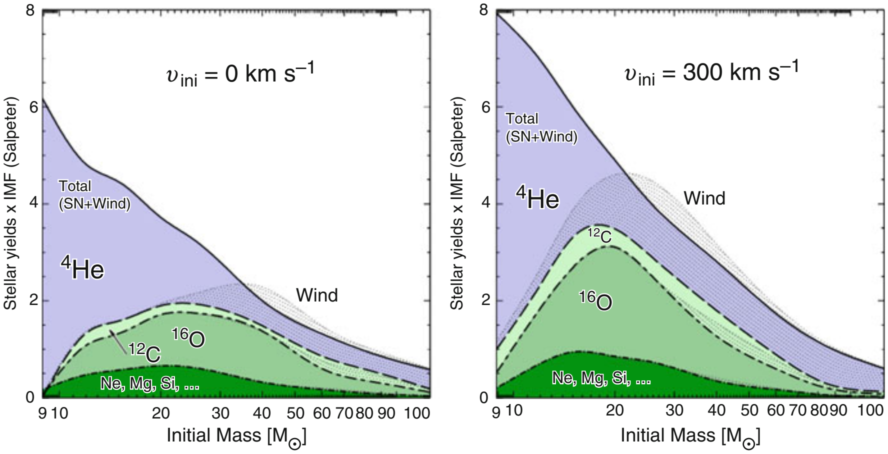

Fig. 15 Product of the stellar yields, $mp_{im}^{\rm tot}$ by Salpeter's IMF (multiplied by an arbitrary constant: 1000×M$^{-2.35}$), as a function of the initial mass for the nonrotating (*left*) and rotating (*right*) models at solar metallicity. The different shaded areas correspond from top to bottom to $mp_{im}^{\rm tot} \times 1000 \times M^{-2.35}$ for ^{4}He, ^{12}C, ^{16}O, and the rest of the heavy elements. The *dotted areas* show for ^{4}He, ^{12}C, and ^{16}O the wind contribution. Preliminary results for masses equal to 9, 85, and 120 $M_\odot$ were used in this diagram (See Hirschi 2004)

mass for the yields of non-rotating models as for the yields of rotating models but shifted to higher masses. Above 30 $M_\odot$, when mass loss dominates, the yields from the rotating models are closer to those of the nonrotating models. The situation for ^{16}O and metallic yields is similar to carbon. Therefore ^{12}C, ^{16}O, and the total metallic yields, Z, are larger for rotating models compared to non-rotating ones by a factor 1.5–2.5 below 30 $M_\odot$.

Figure 15 presents the stellar yields convolved with the Salpeter initial mass function (IMF) ($dN/dM \propto M^{-2.35}$). This reduces the importance of the very massive stars. Nevertheless, the differences between rotating and nonrotating models remain significant, especially around 20 $M_\odot$.

5 Dependence on Metallicity

5.1 Metallicity Effects on General Evolution

The effects of metallicity on stellar evolution are described in several studies (see, e.g., Chieffi and Limongi 2004; Heger et al. 2003; Meynet et al. 1994). A lower metallicity implies a lower luminosity which leads to slightly smaller convective cores. A lower metallicity also implies lower opacity and lower mass losses (as long as the chemical composition has not been changed by burning or mixing in the part of the star one considers). So at the start of the evolution, lower metallicity stars are more compact and thus have bluer tracks during the main sequence. The lower metallicity models also have a harder time reaching the red supergiant (RSG) stage (see Maeder and Meynet 2001, for a detailed discussion). Non-rotating models around $Z = 10^{-3}$ becomes a RSG only after the end of core He burning, and lower metallicity non-rotating models never reach the RSG stage. At even lower metallicities, as long as the metallicity is above about $Z = 10^{-10}$, no significant differences have been found in nonrotating models. Below this metallicity and for metal-free stars, the CNO cycle cannot operate at the start of H burning. At the end of its formation, the star therefore contracts until it starts He burning because the pp chains cannot balance the effect of the gravitational force. Once enough carbon and oxygen are produced, the CNO cycle can operate, and the star behaves like stars with $Z > 10^{-10}$ for the rest of the main sequence. Shell H burning still differs between $Z > 10^{-10}$ and metal-free stars. Metal-free stellar models are presented in Chieffi and Limongi (2004), Umeda and Nomoto (2005), Ekström et al. (2008), and Heger and Woosley (2010).

5.2 Effects of Rotation at Subsolar Metallicities

How does rotation change this picture? At all metallicities, rotation usually increases the core sizes, the lifetimes, the luminosity, and the mass loss. Maeder and Meynet (2001) and Meynet and Maeder (2002a) show that rotation favors a redward evolution and that rotating models better reproduce the observed ratio of blue to red supergiants (B/R) in the Small Magellanic Cloud. Rotating models around $Z = 10^{-5}$ become RSGs during shell He burning. This does not change the ratio B/R but changes the structure of the star when the SN explodes. At even lower metallicities ($Z = 10^{-8}$ models presented in Hirschi 2007), the 20 $M_{\odot}$ models do not become RSG. However, more massive models do reach the RSG stage, and the 85 $M_{\odot}$ model even becomes a WR star of type WO (see below). Maeder and Meynet (2001) also find that a larger fraction of stars reach break-up velocities during the evolution. This will be further discussed in Sect. 5.2.2).

5.2.1 Rotation-Induced Mixing and Production of Primary ^{22}Ne and ^{14}N

Meynet and Maeder (2002a,b) and Hirschi (2007) find that rotating stars produce important amounts of primary ^{14}N and ^{22}Ne via rotation-induced mixing. The production of these nuclei originates from the transport of matter between the He-burning core and the H-burning shell. If the He-burning products ^{12}C and ^{16}O reach the proton-rich layers, they are burnt immediately into ^{14}N via the CNO cycle. A ^{14}N-rich zone is produced in this way at the lower edge of the H-burning shell as shown in Fig. 16. Some of this nitrogen is transported back into the He-burning core, where it is further transformed into ^{22}Ne via two α-captures.

The transport of chemical elements is illustrated for the $25 M_{\odot}$ model with rotation at $Z = 10^{-5}$ in Fig. 16, which shows the abundance profiles in this model during core He burning. The rotation-induced mixing, which leads to the production of primary ^{14}N and ^{22}Ne, occurs in the region above the convective He core

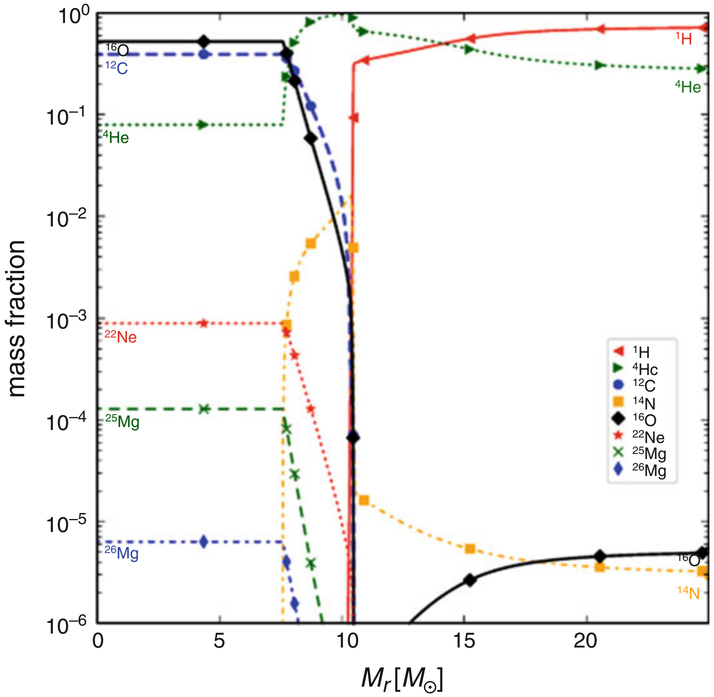

Fig. 16 Abundance profiles of the main light isotopes during central He-burning (X_c(He) ≈ 0.08) for the $25\,M_\odot$ model with rotation and $Z = 10^{-5}$ (C25S4). The convective He-burning core extends from the center to about $M_r = 7.5\,M_\odot$ (flat abundance profiles). The bottom of hydrogen-shell burning is just above $10\,M_\odot$ (sudden drop of hydrogen abundance). Rotation-induced mixing brings freshly produced ^{12}C and ^{16}O from the core into contact with the hydrogen-burning shell, where a peak a primary nitrogen (^{14}N) develops. Further mixing (both convective and rotation induced) brings the primary nitrogen down into the He-burning core where it is transformed into ^{22}Ne, leading to primary production of both ^{14}N and ^{22}Ne Frischknecht et al. (Figure taken from 2016)

($M_r \approx 7.5 - 10.5\,M_\odot$). The core itself is identifiable by the flat abundance profile between $M_r = 0$ and $7.5\,M_\odot$. Differential rotation develops between the convective He core and H shell mainly because of the core contraction and envelope expansion at the end of the main sequence. The differential rotation induces secular shear mixing in this radiative zone, in which no mixing would take place in nonrotating models. Shear mixing, a diffusive process, brings primary ^{12}C and ^{16}O (blue dashed and black continuous lines) into contact with the H-burning layer and creates a ^{14}N-pocket ($M_r \approx 7.5 - 10.5\,M_\odot$) via the CNO cycle as explained above. In our models, the transport of ^{14}N back to the center is mainly due to the growth of the convective core, incorporating parts of the ^{14}N-pocket. Indeed, the diffusive transport is not fast enough to produce a ^{22}Ne mass fraction, $X(^{22}\text{Ne})$, of 10^{-3} to 10^{-2} in the core, necessary to boost the s-process significantly. Although the amount of mixing depends on the prescriptions used for rotation-induced mixing, Frischknecht et al. (2012, 2016) find a production of significant amounts of both ^{14}N and ^{22}Ne in models of various mass and metallicity. Rotational mixing also influences strongly the mass loss of very massive stars as is discussed below.

5.2.2 Mass Loss Due to Critical Rotation and Rotation-Induced Mixing

Mass loss becomes gradually unimportant as the metallicity decreases in the 20 $M_\odot$ models. At solar metallicity, the rotating 20 $M_\odot$ model loses more than half of its mass; at $Z = 0.001$, the 20 models presented in Hirschi (2007) lose less than 15% of their mass; at $Z = 10^{-5}$, less than 3%, and at $Z = 10^{-8}$, less than 0.3%. Meynet et al. (2006) show that the situation can be very different for a 60 $M_\odot$ star at $Z = 10^{-8}$. Indeed, their 60 $M_\odot$ model loses about half of its initial mass. About 10% of the initial mass is lost when the surface of the star reaches break-up velocities during the main sequence. The largest mass loss occurs during the red supergiant (RSG) stage due to the mixing of primary carbon and oxygen from the core to the surface through convective and rotational mixing. The large mass loss is due to the fact that the star crosses the Humphreys–Davidson limit and a high mass loss is used in this phase.

In models from Hirschi (2007) with $\upsilon_{\rm ini} = 600$–$800\,{\rm km\,s^{-1}}$ and $Z = 10^{-8}$, the 20 $M_\odot$ model only reaches break-up velocities at the end of the main sequence (MS) and therefore does not lose mass due to this phenomenon. However, more massive models reach critical velocities early during the MS (the earlier the more massive the model). The mass lost due to breakup increases with the initial mass and amounts to 1.1, 3.5, and 5.5 $M_\odot$ for the 40, 60, and 85 $M_\odot$ models, respectively, in that study. At the end of core H burning, the core contracts and the envelope expands, thus decreasing the surface velocity and $\Omega/\Omega_{\rm crit}$. The mass loss rates becomes very low again until the star crosses the HR diagram and reaches the RSG stage. At this point, the convective envelope dredges up CNO elements to the surface increasing its overall metallicity. In general (see 2.2), the total metallicity, Z, is used (including CNO elements) for the metallicity dependence of the mass loss for the RSG phase. Therefore depending on how much CNO is brought up to the surface, the mass loss can become very large again. The CNO brought to the surface comes from primary C and O produced in He burning. As described in the above subsection, rotational and convective mixing brings these elements into the H-burning shell. A large fraction of the C and O is then transformed into primary nitrogen via the CNO cycle. Additional convective and rotational mixing is necessary to bring the primary CNO to the surface of the star. The whole process is complex and depends on mixing.

Of particular importance is the surface convective zone, which appears when the star becomes a RSG. This convective zone dredges up the CNO to the surface. For a very large mass loss to occur, it is necessary that the star becomes a RSG in order to develop a convective envelope. It is also important that the extent of the convective envelope is large enough to reach the CNO-rich layers. Finally, the star must reach the RSG stage early enough (before the end of core He burning) so that there will be time remaining to lose mass. Models up to about 40 $M_\odot$ in Hirschi

(2007) reach the RSG stage only after the end of helium burning, so too late for a large mass loss. The 60 $M_\odot$ model reaches the RSG stage during He burning. It would therefore have time to lose large amounts of mass. However, the dredge up is not strong enough. The 85 $M_\odot$ model becomes a RSG during He burning earlier than the 60 $M_\odot$ model. The dredge-up is stronger for this model, and the surface CNO abundance becomes very high (see Fig. 17 *bottom*).

The dependence on mixing of the lower initial mass for a large mass loss to occur can be estimated by comparing the 60 $M_\odot$ model calculated in Hirschi (2007) and the one presented by Meynet et al. (2006). The model calculated by Meynet et al. (2006), which does not include overshooting and uses a different prescription for the horizontal diffusion coefficient, D_h (Maeder 2003), loses a large fraction of its mass (and becomes a WR star with high effective temperature) just before the end of core helium burning (see Fig. 4 from Meynet et al. 2006). The D_h used in Meynet et al. (2006), compared to the D_h used in Hirschi (2007), tends to allow a larger enrichment of the surface in CNO-processed elements. This different physical ingredient explains the differences between the two 60 $M_\odot$ models. The fact that, out of two 60 $M_\odot$ models, one model does not lose much mass and the other model with a different physics just does, means that the minimum initial mass for the star to lose a large fraction of its mass is probably around 60 $M_\odot$.

This means that despite expectations that stars at low metallicities have negligible stellar wind contribution to nucleosynthesis, rotation-induced mixing changes the picture and may lead to a significant contribution from stellar winds (due to critical rotation and CNO enrichment of the surface). As at higher metallicities, the stellar wind contribution is limited to H- and He-burning products, in particular CNO elements. This contribution is interesting to explain carbon-enhanced extremely metal-poor stars (see Hirschi 2007, for a discussion on this topic).

6 Weak s-Process

The classic view of the s-process nucleosynthesis in massive stars is that it occurs in He- and C-burning regions of the stars, producing only the low mass range of the s-process elements, typically the elements with an atomic mass number below about 90–100 (see Käppeler et al. 2011, for a review of the topic). It has also been shown that in the regions where the s-process occurs, the fact that, when the metallicity decreases, (1) the neutron source, mainly the $^{22}\mathrm{Ne}(\alpha, n)$ reaction, decreases; (2) the neutron seeds (Fe) also decreases; and (3) the neutron poisons as for instance ^{16}O remain independent of the metallicity implies that the s-process element production decreases with the metallicity and that there exists some limiting metallicity below which the s-process becomes negligible. This limit was found to be around $Z/\mathrm{Z}_\odot=10^{-2}$ (Prantzos et al. 1990), and the process has a metallicity dependence that is even steeper than for secondary processes (see, e.g., Raiteri et al. 1992). The models and plots presented in this section on the weak s-process are taken from a large grid of models including a comprehensive nuclear network of about 700 isotopes from hydrogen to bismuth calculated with GENEC and

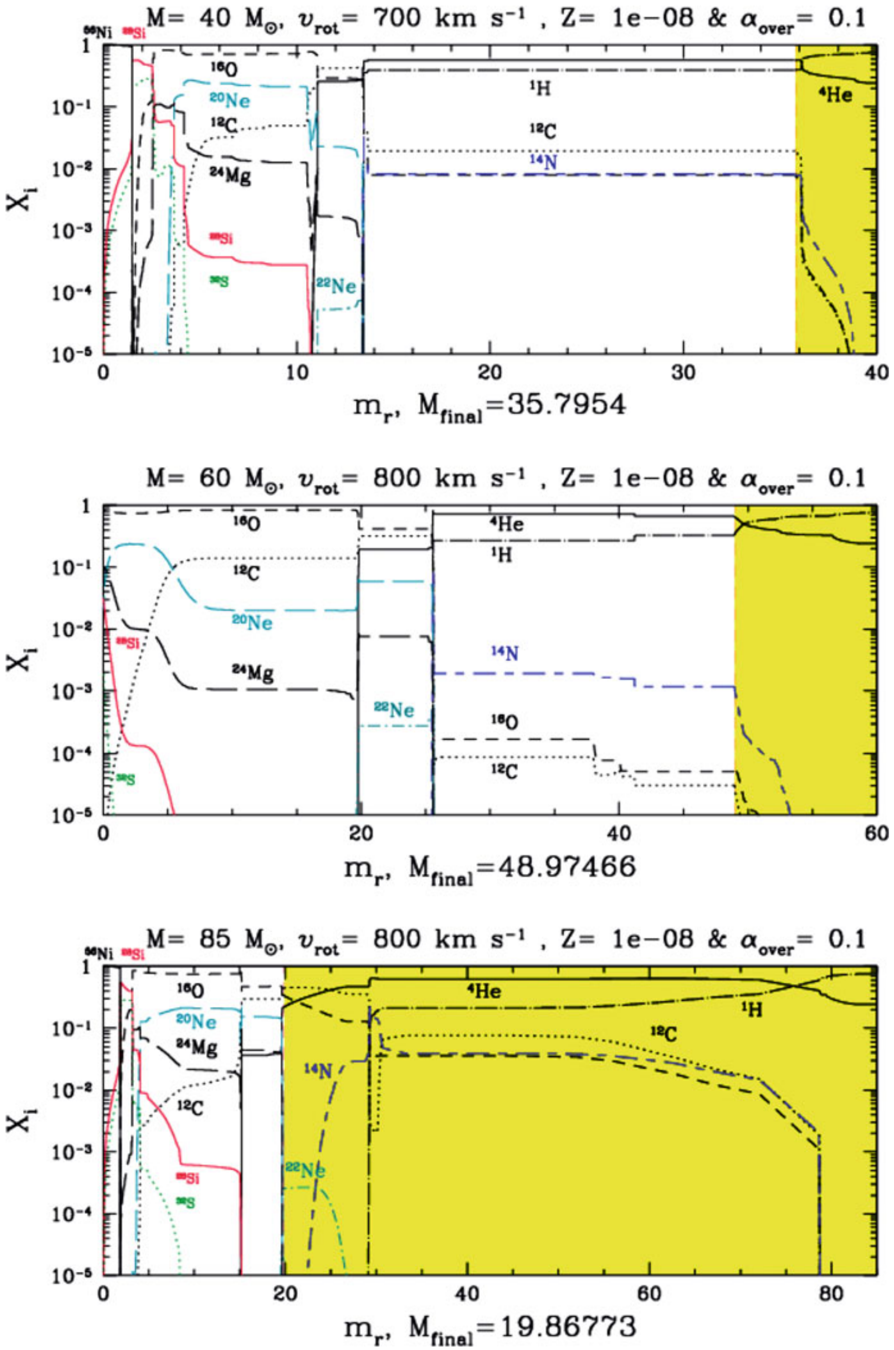

Fig. 17 Abundance profiles for the 40 (*top*), 60 (*middle*), and 85 (*bottom*) $M_\odot$ models. The pre-SN and wind (*yellow-shaded area*) chemical compositions are separated by a *red dashed line* located at the pre-SN total mass (M_{final}), given below each plot (Figure taken from Hirschi 2007)

published in Frischknecht et al. (2012) (25 $M_\odot$ models at various metallicities) and Frischknecht et al. (2016) (15 to 40 $M_\odot$ models at various metallicities). Unless otherwise stated, figures in the section as taken from Frischknecht et al (2012, 2016)

6.1 Standard Weak s-Process in (Nonrotating) Massive Stars

Before discussing the impact of rotation, we first review the standard weak s-process in massive stars at various metallicities and then present recent models in which rotation-induced mixing leads to a strongly enhanced production of s-process at subsolar metallicities compared to nonrotating models.

6.1.1 He Core Burning

The CNO cycle transforms most of the initial $C + N + O$ into ^{14}N. At the beginning of the core He-burning phase, this ^{14}N is converted into ^{22}Ne via two alpha-particle captures. Near the end of helium burning, ^{22}Ne is destroyed by the two reactions $^{22}\mathrm{Ne}(\alpha,n)^{25}\mathrm{Mg}$ and $^{22}\mathrm{Ne}(\alpha,\gamma)^{26}\mathrm{Mg}$. When the temperatures for an efficient activation of $^{22}\mathrm{Ne}(\alpha,n)^{25}\mathrm{Mg}$ are reached, some ^{22}Ne has already been destroyed by the $(\alpha,\gamma)^{26}\mathrm{Mg}$ reaction. More quantitatively, when $T_8 \approx 2.8$ is reached (temperature, at which the (α,n)-channel starts to dominate), massive stars in the mass range 15–40 $M_\odot$ have a mass fraction $X(^{22}\mathrm{Ne}) = 10^{-2} - 5.0 \times 10^{-3}$ left in the core. Important well-known aspects of the s-process during core He burning are the following:

- Because only a small helium mass fraction, $X(^{4}\mathrm{He})$, is left when $^{22}\mathrm{Ne} + \alpha$ is activated (less than 10% in mass fraction), the competition with other α-captures as the $^{12}\mathrm{C}(\alpha,\gamma)$ and 3α is essential at the end of He burning and will affect the s-process efficiency in core He burning. Note that $^{22}\mathrm{Ne} + \alpha$ reactions are also critical to determine the final ^{12}C at the end of helium burning, which in turn is important to the development of carbon burning (convective or radiative core; see discussion in Sect. 3.4). It is thus very important to include α-captures on ^{22}Ne in massive star calculations, even if one only focuses on the evolution of the structure of massive stars.
- The low amount of $X(^{4}\mathrm{He})$, when the neutron source is activated, means also that not all of ^{22}Ne is burned and a part of it will be left for the subsequent C-burning phase. This depends on the stellar core size. The more massive the core, the more ^{22}Ne is burned and the more efficient is the s-process in core He burning, as can be seen from the increasing number of neutron captures per seed n_c in Table 4 in Frischknecht et al. (2016). This is a well-known behavior already found in previous works (Baraffe and Takahashi 1993; Baraffe et al. 1992; Prantzos et al. 1990; Pumo et al. 2010; Rayet and Hashimoto 2000; The et al. 2000, 2007).
- During the late He-burning stages, the bulk of the core matter consists of ^{12}C and ^{16}O, which are both strong neutron absorbers. They capture neutrons to produce ^{13}C and ^{17}O, respectively. ^{13}C will immediately recycle neutrons via $^{13}\mathrm{C}(\alpha,n)$ in He-burning conditions. Instead, the relevance of ^{16}O as a neutron

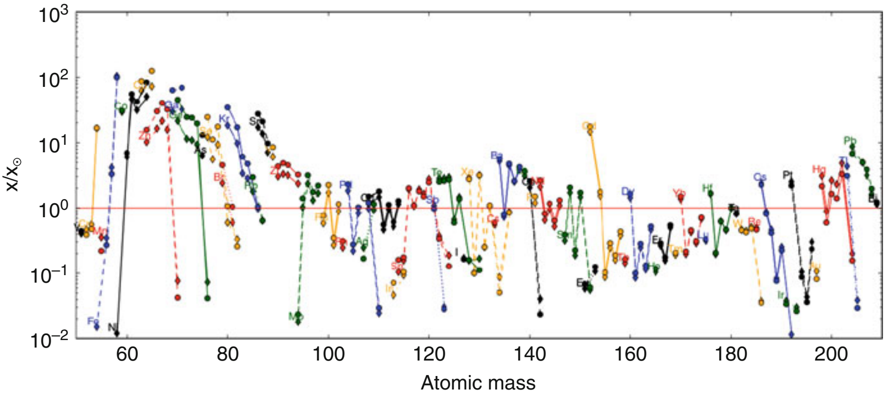

Fig. 18 Isotopic overproduction factors (abundances over initial abundances) of 25 $M_\odot$ models with solar metallicity after He exhaustion. The rotating model (*circles*) has slightly higher factors than the nonrotating model (*diamonds*), but the general production is very similar in both cases and is referred to in the rest of this section as the standard weak s-process

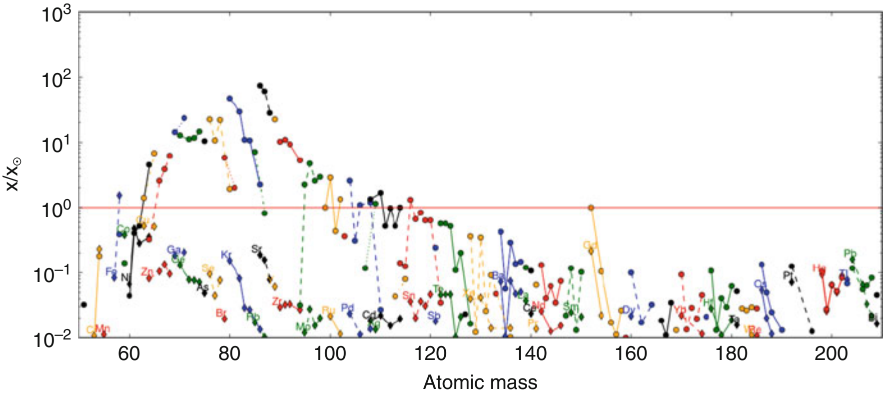

Fig. 19 Isotopic abundances normalized to solar abundances of 25 $M_\odot$ models with with $Z = 10^{-3}$ after He exhaustion. The rotating model (*circles*) has much higher factors than the nonrotating model (*diamonds*)

poison depends on the $^{17}O(\alpha,\gamma)$ and $^{17}O(\alpha,n)$ rates. In particular, the strength of primary neutron poisons, like ^{16}O, increases toward lower metallicities, because of the decreasing ratio of seeds to neutron poisons.

The s-process production in the 25 $M_\odot$ models at solar metallicity is shown in Fig. 18. We will call this production the *standard* weak s-process in the rest of this section. The s-process production for the 25 $M_\odot$ models are shown in Fig. 19 at $Z = 10^{-3}$. Comparing the production of nuclei between $A = 60$ and 90 in nonrotating models between these two metallicities highlights the very strong metallicity dependence of the *standard* weak s-process. As explained above, this is due to the secondary nature of both the neutron source (^{22}Ne$(\alpha, n)^{25}$Mg) and the seeds (mainly iron) (see, e.g., Pignatari and Gallino 2008; Prantzos et al. 1990; Raiteri et al. 1992). During helium burning, the neutron poisons are a mixture of secondary (mainly ^{20}Ne, ^{22}Ne, and ^{25}Mg) and primary (mainly ^{16}O) elements. The s-process production thus becomes negligible below $Z/Z_\odot = 10^{-2}$ (Prantzos et al. 1990), which is already visible in Fig. 19. The decreasing production with decreasing mass is due to the fact that lower mass stars reach lower temperature at the end of He burning. Thus less ^{22}Ne is burnt during He burning (see Table 4 in Frischknecht et al. 2016).

6.1.2 He-Shell Burning

Shell He burning, similarly to the other burning shells, appears at higher temperatures and lower densities than the equivalent central burning phase. High-temperature conditions of $T_8 \approx$ 3.5-4.5 and $\rho \approx$ 3-5.5 $\times$ $10^3\,g\,\mathrm{cm}^{-3}$ cause an efficient ^{22}Ne(α,n) activation for the s-process in shell He burning. However, the highest neutron densities are generally reached only in the layers below the convective shell helium burning. Therefore only a narrow mass range, extending over about $0.2\,M_\odot$ in nonrotating models, at the bottom of the He shell is strongly affected by neutron capture nucleosynthesis. The contribution of the s-process in the He shell amounts to at most $\sim$ 5% of the total s-process yields for the solar metallicity $25\,M_\odot$ (or heavier) model. For less massive stars, the He shell gains more weight and produces in $15\,M_\odot$ models with rotation up to 50% of the total s-process-rich SN ejecta. For 15–20$\,M_\odot$ stars, the He-shell s-process contribution has to be considered (see also Tur et al. 2009).

6.1.3 C-Shell Burning

Shell C burning occurs in the CO core after central C burning. Temperatures and densities at the start of C-shell burning show the same trend with stellar mass as the core burning conditions, i.e., the temperature increases and the density decreases with stellar mass. They vary between $T_9 \approx 0.8$, $\rho \approx 2 \times 10^5\,\mathrm{g\,cm}^{-3}$ in $15\,M_\odot$ models and $T_9 \approx 1.3$, $\rho \approx 8 \times 10^4\,\mathrm{g\,cm}^{-3}$ in $40\,M_\odot$ models. These temperatures are higher than in the central C burning, where $T_9 = 0.6 - 0.8$.

The efficiency of the s-process mainly depends on the remaining iron seeds and ^{22}Ne left after He burning, $X_\mathrm{r}(^{22}\mathrm{Ne})$, in the CO core. All the remaining ^{22}Ne is burned quickly with maximal neutron densities between 6×10^9 and $10^{12}\,\mathrm{cm}^{-3}$. The time scale of this s-process is of the order of a few tens of years in $15\,M_\odot$ stars to a few tenth of a year in $40\,M_\odot$.

A striking difference between the s-process in the He shell and in the C shell is the neutron density, which is much higher in the C shell than in the He shell. The activation of ^{22}Ne(α, n) at the start of C-shell burning leads to a short neutron burst with relatively high neutron densities (typically $n_n \sim 10^{10} - 10^{12}\,\mathrm{cm}^{-3}$; see The et al. 2000, 2007), compared to He burning ($n_n \sim 10^5 - 10^7\,\mathrm{cm}^{-3}$).

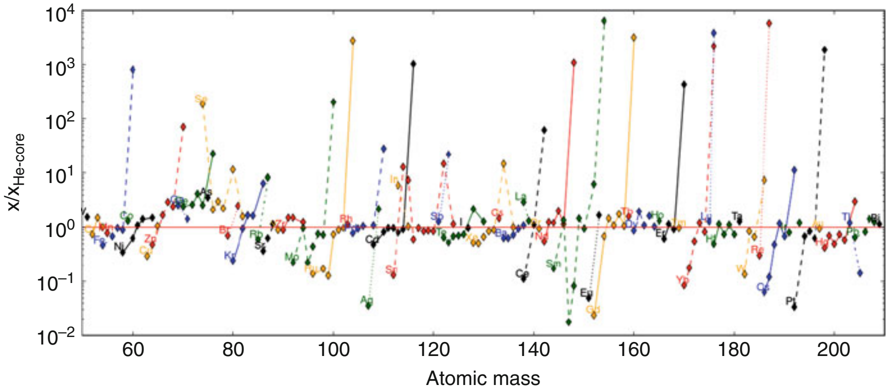

Fig. 20 Ratio of abundances after shell C burning to the abundances after core He burning, $X_{\mathrm{C}}/X_{\mathrm{He}}$, in a nonrotating $25\,M_{\odot}$ star at $Z = \mathrm{Z}_{\odot}$. It illustrates the modification of the abundances by s-process in shell C burning

This leads to a different s-process nucleosynthesis than during the He-shell burning. The ratio of abundances after shell C burning to the abundances after core He burning, $X_{\mathrm{C}}/X_{\mathrm{He}}$ is plotted for the nonrotating $25\,M_{\odot}$ model at $Z = \mathrm{Z}_{\odot}$ in Fig. 20. We can see an overproduction of most isotopes from Zn to Rb. The overproduction during C-burning shell is also found in models of other initial mass, which have both $X_{\mathrm{r}}(^{22}\mathrm{Ne}) \sim 10^{-3}$ and $X(^{56}\mathrm{Fe}) \sim 10^{-4}$, at the start of shell C burning. Mostly 15–25 $M_{\odot}$ stars at solar Z have a strong C-shell contribution in terms of neutron exposure.

In the mass range $A = 60$–90, there are several branching points at ^{63}Ni, ^{79}Se, and ^{85}Kr, respectively. The high neutron densities modify the s-process branching ratios, in a way that the neutron capture on the branching nuclei are favored over the $\beta-$decay channel (see, e.g., Pignatari et al. 2010, and references therein). As a consequence of this, isotopic ratios like ^{63}Cu/^{65}Cu, ^{64}Zn/^{66}Zn, ^{80}Kr/^{82}Kr, ^{79}Br/^{81}Br, ^{85}Rb/^{87}Rb, and ^{86}Sr/^{88}Sr are lowered. Overall, stars with different initial masses show very different final branching ratios. For instance, stars with $15\,M_{\odot}$ and with $20\,M_{\odot}$ (without rotation) produce ^{64}Zn, ^{80}Kr, and ^{86}Sr in the C shell, while in heavier stars, these isotopes are reduced compared to the previous He core.

The impact of the high neutron densities during C shell can be seen in Fig. 20. It causes up to three orders of magnitude overproduction of some r-process nuclei, such as ^{70}Zn, ^{76}Ge, ^{82}Se, or ^{96}Zr, compared to the yields of the "slower" s-process during He burning. However, the production of r-only nuclei in carbon burning compensates only the destruction in the He-core s-process when looking at the final yields. Only for the $40\,M_{\odot}$ model is ^{96}Zr weakly produced.

During C burning, the main neutron poisons are ^{16}O, ^{20}Ne, ^{23}Na, and ^{24}Mg, which are all primary. Thus the C-shell contribution to the s-process will vanish at low metallicities even faster than during He burning. In nonrotating stellar models with $Z < \mathrm{Z}_{\odot}$, the C-burning shell has a small contribution ($< 10\%$).

Many aspects of this phase depend on the rates of a few key nuclear reactions. First, how the shells proceed depends on whether central C burning takes place in a radiative or a convective core. It is thus sensitive to the C/O ratio in the core after He burning and therefore to the $^{12}C(\alpha,\gamma)$ rate. The uncertainty of this rate and its impact on the stellar structure evolution were studied, for example, in Imbriani et al. (2001), El Eid et al. (2004), and Tur et al. (2009). Second, the s-process nucleosynthesis depends on the number of free α particles present in the shell that can trigger neutron production by $^{22}Ne(\alpha,n)$ (Raiteri et al. 1991) or $^{13}C(\alpha,n)$ (Bennett et al. 2012; Pignatari et al. 2013). In carbon burning, α particles are released by the $^{12}C+^{12}C$ α-channel. The following studies by Limongi et al. (2000), Rauscher et al. (2002), The et al. (2007), and Pignatari et al. (2010) confirmed that $^{22}Ne(\alpha,n)$ is the only important neutron source in C-shell burning, where the remaining ^{22}Ne left after central He burning is consumed in a very short time (time scale ∼1 year). At shell C-burning temperatures ($T_9 \sim 1$), the ratio of the $^{22}Ne(\alpha,n)$ to $^{22}Ne(\alpha,\gamma)$ rates is about 230. In these conditions, the main competitor is the $^{22}Ne(p,\gamma)$, where protons are made by the C-fusion channel $^{12}C(^{12}C,p)^{23}Na$. Alternatively, Bennett et al. (2012) and Pignatari et al. (2013) showed that for $^{12}C+^{12}C$ larger than about a factor of 100 compared to the CF88 rate at typical central C-burning temperatures, the $^{13}C(\alpha,n)^{16}O$ reaction activated in the C core may strongly affect the final s-process yields. The $^{12}C+^{12}C$ rate needs to be better constrained by experiments (e.g., Wiescher et al. 2012). Other neutron sources such as $^{17}O(\alpha,n)$ and $^{21}Ne(\alpha,n)$ recycle most of the neutrons absorbed by ^{16}O and ^{20}Ne, respectively (e.g., Limongi et al. 2000).

6.2 Impact of Rotation on the s-Process

Rotation significantly changes the structure and pre-SN evolution of massive stars (Hirschi et al. 2004) and thus also the s-process production. Rotating stars have central properties similar to more massive nonrotating stars. In particular, they have more massive helium burning and CO cores (see Sect. 3), respectively, which is an effect of rotation also found by other studies (e.g., Chieffi and Limongi 2013; Heger and Langer 2000). Our models with rotation show typically 30%–50% larger He cores and CO cores than the nonrotating models. A $20\,M_{\odot}$ star with rotation has thus a core size which is almost as large as the one of a $25\,M_{\odot}$ nonrotating star. The higher core size means higher central temperatures at the same evolutionary stage and consequently the $^{22}Ne+\alpha$ is activated earlier. In these conditions, the He-core s-process contribution increases at the expense of the C-shell contribution. Since in He-burning conditions the amount of neutrons captured by light neutron poisons and not used for the s-process is lower compared to C-burning conditions, an overall increase of the s-process efficiency is obtained (see also Pignatari et al. 2010). Early investigations of the possible role of rotational mixing on the s-process production in massive stars have shown that this classic picture could be significantly revised (Hirschi 2007; Hirschi et al. 2008; Pignatari et al. 2008). Following these initial studies, the impact of rotation on the s-process nucleosynthesis in low-Z massive rotating stars was studied in detail by Frischknecht et al. (2012, 2016).

In addition to rotating models having higher core masses and thus higher core temperature, s-process production is also increased due to additional production of ^{22}Ne via rotation-induced mixing. Rotational mixing allows the production of large amounts of ^{14}N in the H-burning shell, ^{14}N, which, once engulfed into the He-burning core, is transformed into ^{22}Ne via two $\alpha-$captures (see Frischknecht et al. 2016; Hirschi 2007, for details). Increasing the quantity of ^{22}Ne favors s-process production since the main neutron source is the ^{22}Ne(α, n) reaction. The amount of iron seeds and neutron poisons is not affected by rotation. Thus rotation acts mainly on one of the aspects of the s-process nucleosynthesis, the neutron source via the amount of ^{22}Ne.

At solar metallicity, the difference between rotating and nonrotating stars is mainly found in the core size, but not in the amount of available ^{22}Ne. The difference in s-processing between rotating and nonrotating stars is the smallest at $25\,M_{\odot}$, when comparing 15–25$\,M_{\odot}$ models. It is related to the saturation of the s-process toward higher core/initial masses, which was already found by Langer et al. (1989). In Fig. 18, the overproduction factors of $25\,M_{\odot}$ rotating and nonrotating models at solar metallicity after the end of He burning are shown. The rotating model (circles) shows only a moderate increase of the s-process production with respect to the nonrotating model (diamonds). Both models produce heavy isotopes from iron seeds up to the Sr-peak ($A \approx 90$). The varying overproduction factors ($\neq 1$) beyond $A = 90$ are the signature of a local redistribution of pre-existing heavy nuclei. This figure therefore illustrates that not only the s-process quantitative production is similar but also the abundances pattern of rotating and nonrotating models at solar Z are almost identical. The difference in the efficiency is mostly caused by the larger core size in the rotating models.

6.2.1 Impact of Rotation on the s-Process at Low Metallicities

At subsolar metallicities, the differences between rotating and nonrotating models are much more striking. Rotating models have much higher neutron exposures compared to nonrotating stars, which is due to the primary ^{22}Ne produced and burned during central He burning. In the models published in Frischknecht et al. (2016), 3–270 times higher amount of ^{22}Ne burned in rotating stars up to central He exhaustion, depending on the initial mass (or $M_{\rm CO}$) and metallicity. The large production of neutrons by ^{22}Ne is partially compensated by the larger concentration of ^{25}Mg and ^{22}Ne itself, which become primary neutron poisons in rotating massive stars (Pignatari and Gallino 2008). Figure 19 shows the abundance normalized to solar in the CO core of $25\,M_{\odot}$ stars with $Z = 10^{-3}$ just after central He exhaustion, each for a rotating (circles) and a nonrotating model (diamonds). Corresponding plots for $Z = 10^{-5}$ and $Z = 10^{-7}$ can be found in Frischknecht et al. (2016). Going from $Z = Z_{\odot}$ (Fig. 18) to $Z = 10^{-3}$ (Fig. 19) and lower Z, the production of nuclei between $A = 60$ and 90 vanishes in the nonrotating models, which is what is expected from the combination of secondary neutron source, secondary seeds,

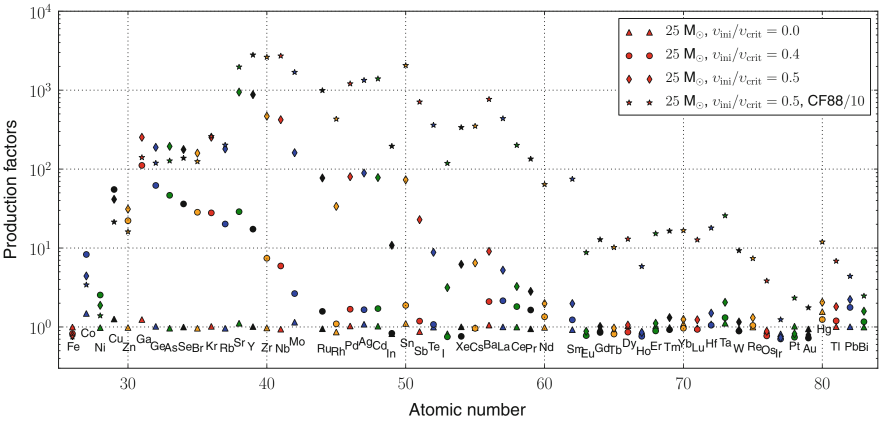

Fig. 21 Production factors (ejected mass divided by the initial mass of the element) for the 25 $M_\odot$ models with $Z = 10^{-5}$ after the end of core He burning. The model without rotation (*triangles*) does not produce s-process efficiently, whereas the rotating models (*circles*, B1 and *diamonds*, B3) do. The additional rotating models with reduced $^{17}\mathrm{O}(\alpha,\gamma)$ rates (*stars*, B4, CF88/10) highlight the uncertainty for the neutron poison $^{16}\mathrm{O}$

and primary neutron poisons. On the other hand, the rotating models at subsolar Z produce efficiently up to Sr ($Z = 10^{-3}$), Ba ($Z = 10^{-5}$) and finally up to Pb ($Z = 10^{-7}$). At the same time, the consumption of iron seeds increases from 74% at $Z = \mathrm{Z}_\odot$ to 96%, 97% and 99% at $Z = 10^{-3}$, $Z = 10^{-5}$, and $Z = 10^{-7}$, respectively, for 25 $M_\odot$. Also with the standard rotation rate $\upsilon_{\rm ini}/\upsilon_{\rm crit} = 0.4$, around 90% of initial Fe is destroyed in models with $25\,M_\odot$ and $Z < \mathrm{Z}_\odot$. Hence already from the s-process in He burning, one can conclude that the primary neutron source in the rotating models is sufficient to deplete all the seeds and the production is limited by the seeds (not the neutron source any more). The other stellar masses show similar trends with Z.

This explains why the s-process yields are much larger in the rotating model, by up to a factor of 1000. Nevertheless, at $Z = 10^{-3}$ (or [Fe/H] $= -1.8$), rotating models produce elements in large quantities only up to the Sr peak. We hence expect that the rotation-enhanced s-process to be qualitatively similar the normal s-process (production of elements with $A = 60$–90) for [Fe/H] > -2 but with higher production factors. At $Z = 10^{-5}$ (or [Fe/H]$= -3.8$; see Fig. 21 showing production factors at the pre-SN stage), elements up to Sr are still strongly produced in the rotating model (circles in Fig. 21), whereas in the nonrotating model, the overproduction is very small. Depending on the initial rotation rate and the $^{17}\mathrm{O}(\alpha,\gamma)$ rate used, elements up to Ba start to be efficiently produced (see discussion below). At $Z = 10^{-7}$ (or [Fe/H] $= -5.8$), both the rotating and nonrotating models produce and burn enough $^{22}\mathrm{Ne}$ to deplete all the iron seeds. At this very low Z, the main limitation is the seeds, and, given the low initial iron content, the s-process production remains very modest.

It is interesting to look at the metallicity dependence of the rotation-enhanced s-process production in rotating models. As said above, the production is limited mainly by the iron seeds. Even at the lowest metallicities in a very fast-rotating model ($\upsilon_{\text{ini}}/\upsilon_{\text{crit}} = 0.6$ instead of the standard 0.4), and thus with a larger primary neutron source, there is no additional production of s-process elements starting from light element seeds like ^{22}Ne. Instead, what happens is that not only iron is depleted but elements up to Sr are partially destroyed (after being produced) and heavier elements like Ba are produced ([Sr/Ba]$\leq$0). Indeed, going from [Fe/H]$= -3.8$ to [Fe/H]$= -5.8$, the Sr yield decreases by a factor of $\sim$ 9, while the Ba yield increases by a factor of 5 (see Table 1 in Frischknecht et al. 2012). We therefore have a different metallicity dependence for the production of elements belonging to the different peaks: there is a roughly secondary production of elements up to Sr, but the Z dependence for heavier elements like Ba is milder. The secondary-like behavior of Sr/Y/Zr in the metallicity range covered makes the nonstandard s-process in massive rotating stars an unlikely solution for the LEPP (light element primary process) problem at low Z (Travaglio et al. 2004).

Apart from the seeds, the s-process is strongly dependent on the neutron source and neutron poisons. Both are still quite uncertain at present. The neutron source, ^{22}Ne, depends on rotation-induced mixing and thus on the initial velocity of stars at very low Z. In models calculated with a higher initial velocity ($\upsilon_{\text{ini}}/\upsilon_{\text{crit}} = 0.5$–$0.6$ instead of 0.4), the increase in the production of ^{22}Ne is about a factor of 4. This leads to a higher neutron capture per seed (n_c) and thus to a production of elements like Ba at the expense of elements like Ge, but the total production (sum of all isotopes heavier than iron) is still limited by the iron seeds as said above. A major uncertainty concerning neutron poisons is the importance of ^{16}O as a neutron poison. At low Z, ^{16}O is a strong neutron absorber during core He burning. The neutrons captured by $^{16}\text{O}(n,\gamma)^{17}\text{O}$ may either be recycled via $^{17}\text{O}(\alpha,n)^{20}\text{Ne}$ or lost via $^{17}\text{O}(\alpha,\gamma)^{21}\text{Ne}$. The impact of the $^{17}\text{O}(\alpha,\gamma)^{21}\text{Ne}$ uncertainty can be seen by comparing the diamonds and stars (models with the CF88 rate divided by a factor of 10) in Fig. 21. The impact of a change of even a factor of 10 in this rate is strong. Given the differences between models with the CF88 and CF88/10 rate, the experimental determination of the $^{17}\text{O}(\alpha,\gamma)$-rate and the $^{17}\text{O}(\alpha,n)$ is crucial to give a more accurate prediction for the s-process in massive rotating stars at low metallicity. Note the more precise determination of $^{22}\text{Ne}(n,\gamma)$ and $^{22}\text{Ne}(\alpha,\gamma)$ is also important (Nishimura et al. 2014).

6.2.2 Relative Contributions and Total Yields

The following points can be derived concerning the relative contributions from for He-core, C-shell, and He-shell burning to the total yields (see Fig. 13 in Frischknecht et al. 2016, for the production of ^{68}Zn):

1. In general, the contribution from He-core burning dominates over the other two phases overall.
2. Shell carbon burning is, compared to the other two sites, only efficient at solar metallicity. The weak contribution from the C shell at low-Z is due to the

low amount of ^{22}Ne left, the smaller amount of seeds, and the primary neutron poisons, which have an increased strength toward lower Z in C-shell conditions. The only mass-metallicity range for which the C shell dominates is at solar Z with $M \lesssim 25\,M_\odot$ for nonrotating models and with $M \lesssim 20\,M_\odot$ for rotating models. Such a dominant contribution from C shell was not seen in previous literature (e.g., The et al. 2007). This may be due to the high ^{22}Ne(α,γ) rate of NACRE, which is in strong competition to the neutron source during central He burning and dominates for stars with $M \lesssim 20\,M_\odot$. This inhibition during He-core burning is weaker for rotating stars since they have higher central temperatures.

3. Shell He burning contributes only a small fraction but typically 5% to the final yields. The exceptions are the rotating 15–25 $M_\odot$ stars at low Z and rotating 15–20 $M_\odot$ stars at solar Z. It is the effect of decreasing contribution from the He core toward lower masses and the higher burning temperatures in the shell compared to the He core, which allows an efficient activation of ^{22}Ne(α,n) in the 15 $M_\odot$ models. Additionally the He shell is not limited by the diminished iron seeds consumed by s-process in He core but occurs in a region still containing its initial iron content.

In Fig. 22, the dependence of total ^{88}Sr yields on the mass and metallicity are displayed for rotating stars with standard rotation rate ($\upsilon_{\rm ini}/\upsilon_{\rm crit} = 0.4$) (*right*) and for nonrotating stars (*left*). The red circles display the location of the models computed in the mass-metallicity space. The values in between the data points are interpolated linearly in $\log(m)$. This plot for the neutron-magic isotope ^{88}Sr shows the dependence of the Sr-peak production on rotation (^{86}Sr, ^{87}Sr, ^{89}Y, and ^{90}Zr show the same trends as ^{88}Sr). Several differences between the standard and rotation boosted s-process can be seen:

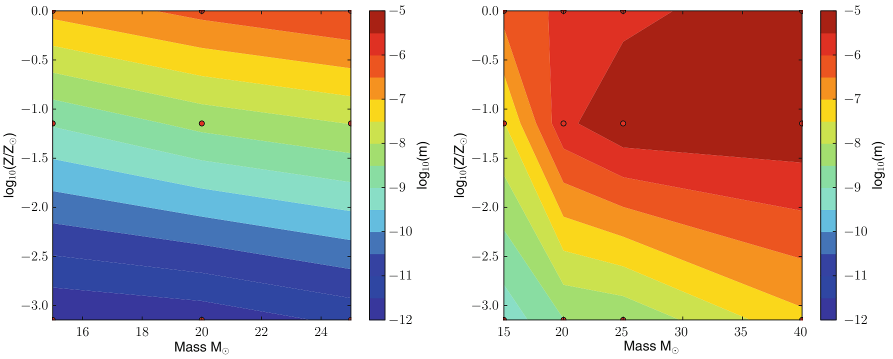

Fig. 22 s-process yields, m, of ^{88}Sr in $M_\odot$ to illustrate the mass and metallicity dependence of the s-process, without rotation (*left*) and with rotation (*right*). The *red circles* display the location of the models computed in the mass-metallicity space. The values in between the data points are interpolated linearly in $\log(m)$

1. Rotating models clearly produce more s-process elements at all metallicities.
2. Whereas the s-process production in nonrotating model decreases steeply with metallicity (dependence steeper than linear, e.g., Pignatari and Gallino 2008), the ^{68}Zn yields (discussed above as a typical weak s-process element) of rotating stars show a secondary-like behavior, going from reddish to blueish colors toward lower Z. While the ^{68}Zn yields of nonrotating stars drop by five orders of magnitude when the metallicity goes down by a factor 10^3, the yields from rotating stars drop only by a factor 10^3. The scaling with metallicity is less steep for rotating models (see Fig. 13 in Frischknecht et al. 2016).
3. Furthermore, the Sr-peak isotopes do not show a secondary behavior for stars with rotation and $M > 15\,M_\odot$ in the metallicity range between solar ($\log(Z/Z_\odot) = 0$) and about one hundredth ($Z = 1.4 \times 10^{-4}$, $\log(Z/Z_\odot) = -2$) of solar metallicity, but they eject maximal absolute yields around one tenth of solar metallicity (dark red around $\log(Z/Z_\odot) = -1$) for 20 to 30 $M_\odot$ stars.

Galactic chemical evolution (GCE) models using the larger grid of models were presented in Cescutti et al. (2013, 2015) (with some modifications explained in these papers) and showed that rotation-induced mixing is able to explain the large scatter for [Sr/Ba] observed in extremely metal poor stars. Furthermore, observations of large s-process enhancements in one of the oldest globular clusters in the bulge of our galaxy support the view that massive stars could indeed be also important sources for these elements (Chiappini et al. 2011). The observations by Barbuy et al. (2009) and Chiappini et al. (2011) were later updated by Barbuy et al. (2014) and Ness et al. (2014). In particular, Barbuy et al. (2014) confirmed that at least part of the stars in the globular cluster NGC 6522 are compatible with the s-process production in fast-rotating massive stars at low metallicity.

7 Conclusions

In this chapter, we reviewed the stellar structure equations and pre-supernova evolution of massive stars with a particular emphasis on the effects of rotation and mass loss and the transition between intermediate-mass and massive stars. We then presented the stellar wind contribution to nucleosynthesis and the production of weak s-process at various metallicities. Rotation and mass loss both have a strong impact on the evolution and nucleosynthesis in massive stars. There are broadly two mass ranges, where either rotation-induced mixing dominates for $M < 30M_\odot$ or mass loss dominates for $M > 30M_\odot$ over the other process (see Meynet and Maeder 2003, for more details). Rotation affects the mass limits for the presence of convection during central carbon burning, for iron core collapse supernovae, and for black hole formation. The effects of rotation on pre-supernova models are most spectacular for stars between 15 and 25 $M_\odot$. Indeed, rotation changes the supernova type (IIb or Ib instead of II), the total size of progenitors (blue instead of red supergiant), and the core sizes by a factor ~ 1.5 (bigger in rotating models). For Wolf–Rayet stars ($M > 30M_\odot$) even if the pre-supernova models are not different between rotating and nonrotating models, their previous evolution is different (Meynet and Maeder 2003).

The very strong radiation field of massive stars leads to strong mass loss. Thus massive stars near solar metallicity lose a large fraction of their initial mass, more than half their initial mass for stars more massive than 20 $M_\odot$. Most of the mass loss takes place during hydrogen- and helium-burning phases. This implies that the stellar wind contribution to nucleosynthesis consists mostly of hydrogen-burning products and to a smaller extent helium-burning products, i.e., elements up to aluminum. Observations from the Integral gamma-ray satellite (Diehl et al. 2006) confirm that massive stars in our galaxy produce significant amounts of ^{26}Al, a radioactive element with half-life of $\sim$ 7.2 $\times$ 10^5 years and emitting photons at 1808.65 keV. Rotating models have larger stellar wind contribution to yields than the nonrotating ones because of the extra mass loss and mixing due to rotation. For the pre-SN yields and for masses below $\sim$ 30 $M_\odot$, rotating models have larger yields. The ^{12}C and ^{16}O yields are increased by a factor of 1.5–2.5 by rotation in the present calculation. When we add the two contributions, the yields of most heavy elements are larger for rotating models below $\sim$ 30 $M_\odot$. Rotation increases the total metallic yields by a factor of 1.5–2.5. As a rule of thumb, the yields (and evolution) of a rotating 20 $M_\odot$ star are similar to the yields of a nonrotating 30 $M_\odot$ star, at least for the light elements. When mass loss is dominant (above $\sim$ 30 $M_\odot$) rotating and nonrotating models give similar yields for heavy elements. Only the yields of H-burning products are increased by rotation in the very massive star range.

At low and very low Z, one expects mass loss and the production of secondary elements like ^{14}N to decrease and gradually become negligible. Rotation changes this picture. During the course of helium burning, rotation-induced mixing mixes ^{12}C and ^{16}O into the hydrogen-burning shell where the CNO cycles transform most of the C and O into ^{14}N leading to the production of large amounts of primary nitrogen. For the most massive models ($M \gtrsim 60\ M_\odot$), primary production of CNO elements raises the overall metallicity of the surface drastically, and significant mass loss occurs during the red supergiant stage assuming that CNO elements are important contributors to mass loss. This mass loss is due to the surface enrichment in CNO elements via rotational and convective mixing. Current models predict the production of WR stars for an initial mass higher than 60 $M_\odot$ even at $Z = 10^{-8}$. Therefore SNe of type Ib and Ic are predicted from single massive stars at these low metallicities. The stellar yields of rotating models were used in a galactic chemical evolution model and successfully reproduce the early evolution of CNO elements (Chiappini et al. 2006). Furthermore, fast-rotating massive stars are candidates to explain CEMP-no stars in the early universe (Maeder et al. 2015). (For further discussion of CEMP and CEMP-no stars see ▸ Chap. 73, “Nucleosynthesis in Hypernovae Associated with Gamma Ray Bursts” by Ken’ichi Nomoto in this book.)

The production of primary ^{14}N and also ^{22}Ne in rotating massive stars at low Z opens the door to produce s-process elements at low Z. Large grids of rotating massive star models were recently completed to determine the impact of rotation on slow neutron captures from solar down to very low metallicities (Frischknecht et al. 2016). The main results of these studies are the following:

- Rotation not only enables the production of primary nitrogen but also of important quantities of primary ^{22}Ne at all metallicities. Whereas the neutron source for the s-process in non-rotating models is secondary, the neutron source is primary in rotating models.
- At solar metallicity, rotation-induced mixing increases the weak s-process production but its impact is modest (within a factor of 2) and the production in rotating models stops at the strontium peak as in standard models.
- As the metallicity decreases, the amount of iron seeds decreases, and the iron seeds are the main limitation to the production of heavier elements in rotating models, in which the neutron source is primary. The decreasing amount of seeds does not prevent the production of heavier elements though. On the other hand, the lack of seeds means that not only the seeds get depleted, but elements in the mass range $A = 60$–80 also get depleted as the production peak shifts to the strontium peak by $Z = 10^{-3}$ and elements up to the barium peak are efficiently produced at that metallicity and very low metallicities. The final [Sr/Ba] ratio obtained in the models covers the range between roughly -0.5 and 2.1.
- The strong dependence of production of the barium peak on metallicity and initial rotation rate means that rotating models provide a natural explanation for the observed scatter for the [Sr/Ba] ratio at the low metallicities.
- The general decrease with metallicity of the [Sr/Ba] ratio in rotating models also matches the decreasing ratio observed in the small current sample of CEMP-no stars at extremely low [Fe/H].
- Although they are challenging to measure, isotopic ratios, for example, for magnesium isotopes, have a great potential for constraining stellar models.

There are important uncertainties that affect the results presented in this chapter. On the nuclear side, the dominant uncertainties for the weak s-process are the exit channel ratios between n and γ for alpha captures on ^{17}O and ^{22}Ne. The first ratio determines whether ^{16}O is a strong neutron poison or only a strong absorber, while the second determines the strength of the neutron source $^{22}\mathrm{Ne}(\alpha, n)$. $^{12}\mathrm{C}(\alpha, \gamma)^{16}\mathrm{O}$ and its competition with triple-α and $^{22}\mathrm{Ne}(\alpha, \gamma)$ are key to determine the final abundance of carbon at the end of helium burning. This abundance is a key quantity that affects the evolution throughout the advanced phases.

On the stellar side, the interplay of mean molecular weight and magnetic fields with rotation-induced instabilities and mixing is the main uncertainty. It is not fully clear yet whether magnetic fields would increase or decrease rotation-induced mixing (see Maeder and Meynet 2005; Meynet et al. 2013; Woosley and Heger 2006; Yoon and Langer 2005). The dependence of the mass loss rates on the metallicity, especially in the RSG stage, needs to be further studied to see how the results of van Loon et al. (2005, mass loss in the RSG phase independent of metallicity) can be extrapolated to very low metallicities. The reader is referred to the review by Langer (2012) concerning the evolution of binary stars. Finally, convective boundary mixing (CBM) is still uncertain, and many studies have focused on this uncertainty recently taking advantage of the significant increase in computing power. Important improvements are thus expected in the modelling of massive stars in the years ahead (see Arnett et al. 2015 for more details). Nevertheless, the results presented in this chapter show that a lot of progress has already been made in the modelling of the pre-supernova evolution of massive stars.

8 Cross-References

- ▸ Electron Capture Supernovae from Super Asymptotic Giant Branch Stars
- ▸ Influence of Non-spherical Initial Stellar Structure on the Core-Collapse Supernova Mechanism
- ▸ Nucleosynthesis in Thermonuclear Supernovae
- ▸ Nucleosynthesis in Spherical Explosion Models of Core-Collapse Supernovae
- ▸ Nucleosynthesis in Hypernovae Associated with Gamma Ray Bursts
- ▸ Population Synthesis of Massive Close Binary Evolution
- ▸ Supernovae from Massive Stars
- ▸ Supernovae from Rotating Stars
- ▸ Very Massive and Supermassive Stars: Evolution and Fate

Acknowledgements The author thanks his collaborators at the University of Geneva (G. Meynet, A. Maeder, Sylvia Ekström, and C. Georgy), Basel (U. Frischknecht, F.-K. Thielemann, T. Rauscher), and Hull (M. Pignatari) for their significant contributions to the results presented in this chapter. R. Hirschi acknowledges support from the World Premier International Research Center Initiative (WPI Initiative), MEXT, Japan, and from the Eurogenesis EUROCORE program. The research leading to these results has received funding from the European Research Council under the European Union's Seventh Framework Programme (FP/2007-2013) / ERC Grant Agreement n. 306901. This article is based upon work from the "ChETEC" COST Action (CA16117), supported by COST (European Cooperation in Science and Technology).

References

Arnett WD, Thielemann FK (1985) Hydrostatic nucleosynthesis. I – Core helium and carbon burning. Astrophys J 295:589–619

Arnett WD, Meakin C, Viallet M, Campbell SW, Lattanzio JC, Mocák M (2015) Beyond mixing-length theory: a step toward 321D. Astrophys J 809:30. doi:10.1088/0004-637X/809/1/30, 1503.00342

Baraffe I, Takahashi K (1993) Contribution to the heavy-element abundances in the Galactic halo from s-process nucleosynthesis in massive stars. Astron Astrophys 280:476–485

Baraffe I, El Eid MF, Prantzos N (1992) The s-process in massive stars of variable composition. Astron Astrophys 258:357–367

Barbuy B, Zoccali M, Ortolani S, Hill V, Minniti D, Bica E,Renzini A, Gómez A (2009) VLT-FLAMES analysis of 8 giants in the bulge metal-poor globular cluster NGC 6522: oldest cluster in the Galaxy? Analysis of 8 giants in NGC 6522. Astron Astrophys 507:405–415. doi:10.1051/0004-6361/200912748, 0908.3603

Barbuy B, Chiappini C, Cantelli E, Depagne E, Pignatari M, Hirschi R, Cescutti G, Ortolani S, Hill V, Zoccali M, Minniti D, Trevisan M, Bica E, Gómez A (2014) High-resolution abundance analysis of red giants in the globular cluster NGC 6522. Astron Astrophys 570:A76. doi:10.1051/0004-6361/201424311, 1408.2438

Bennett ME, Hirschi R, Pignatari M, Diehl S, Fryer C, Herwig F, Hungerford A, Nomoto K, Rockefeller G, Timmes FX, Wiescher M (2012) The effect of $^{12}\mathrm{C}+^{12}\mathrm{C}$ rate uncertainties on the evolution and nucleosynthesis of massive stars. Mon Not R Astron Soc 420:3047–3070. doi:10.1111/j.1365-2966.2012.20193.x, 1201.1225

Brüggen M, Hillebrandt W (2001) Three-dimensional simulations of shear instabilities in magnetized flows. Mon Not R Astron Soc 323:56–66

Braithwaite J (2006) A differential rotation driven dynamo in a stably stratified star. Astron Astrophys 449:451–460. doi:10.1051/0004-6361:20054241, arXiv:astro-ph/0509693

Canuto VM (2002) Critical Richardson numbers and gravity waves. Astron Astrophys 384: 1119–1123

Cescutti G, Chiappini C, Hirschi R, Meynet G, Frischknecht U (2013) The s-process in the galactic halo: the fifth signature of spinstars in the early Universe? Astron Astrophys 553:A51 doi:10.1051/0004-6361/201220809, 1302.4354

Cescutti G, Romano D, Matteucci F, Chiappini C, Hirschi R (2015) The role of neutron star mergers in the chemical evolution of the galactic halo. ArXiv e-prints 1503.02954

Chaboyer B, Zahn JP (1992) Effect of horizontal turbulent diffusion on transport by meridional circulation. Astron Astrophys 253:173–177

Chiappini C, Hirschi R, Meynet G, Ekström S, Maeder A, Matteucci F (2006) A strong case for fast stellar rotation at very low metallicities. Astron Astrophys 449:L27–L30. doi:10.1051/0004-6361:20064866, astro-ph/0602459

Chiappini C, Frischknecht U, Meynet G, Hirschi R, Barbuy B, Pignatari M, Decressin T, Maeder A (2011) Imprints of fast-rotating massive stars in the galactic bulge. Nature 472:454–457. doi:10.1038/nature10000

Chieffi A, Limongi M (2004) Explosive yields of massive stars from $Z = 0$ to $Z = Z_{\odot}$. Astrophys J 608:405–410. doi:10.1086/392523

Chieffi A, Limongi M (2013) Pre-supernova evolution of rotating solar metallicity stars in the mass range 13–120 $M\odot$ and their explosive yields. Astrophys J 764:21. doi:10.1088/0004-637X/764/1/21

Chieffi A, Limongi M, Straniero O (1998) The evolution of a 25 Mo star from the main sequence up to the onset of the iron core collapse. Astrophys J 502:737

Cristini A, Meakin C, Hirschi R, Arnett D, Georgy C, Viallet M (2017, submitted) 3D hydrodynamic simulations of the carbon shell in a massive star. MNRAS

Crowther PA (2001) Stellar winds from massive stars. In: Vanbeveren D (ed) The influence of binaries on stellar population studies, astrophysics and space science library. vol 264. Springer, p 215. arXiv:astro-ph/0010581, ISBN:0792371046

Crowther PA, Schnurr O, Hirschi R, Yusof N, Parker RJ, Goodwin SP, Kassim HA (2010) The R136 star cluster hosts several stars whose individual masses greatly exceed the accepted 150Mo stellar mass limit. Mon Not R Astron Soc 408:731–751. doi:10.1111/j.1365-2966.2010.17167.x, 1007.3284

de Jager C, Nieuwenhuijzen H, van der Hucht KA (1988) Mass loss rates in the Hertzsprung-Russell diagram. Astron Astrophys Suppl 72:259–289

Diehl R, Halloin H, Kretschmer K, Lichti GG, Schönfelder V, Strong AW, von Kienlin A, Wang W, Jean P, Knödlseder J, Roques JP, Weidenspointner G, Schanne S, Hartmann DH, Winkler C, Wunderer C (2006) Radioactive ^{26}Al from massive stars in the galaxy. Nature 439:45–47. doi:10.1038/nature04364, astro-ph/0601015

Edelmann PVF, Roepke FK, Hirschi R, Georgy C, Jones S (2017, submitted) Testing a one-dimensional prescription of dynamical shear mixing with a two-dimensional hydrodynamic simulation. Astron Astrophys

Eggenberger P, Meynet G, Maeder A, Hirschi R, Charbonnel C, Talon S, Ekström S (2007) The Geneva stellar evolution code. Astrophys Space Sci 263. doi:10.1007/s10509-007-9511-y

Ekström S, Meynet G, Chiappini C, Hirschi R, Maeder A (2008, accepted) Effects of rotation on the evolution of primordial stars. Astron Astrophys 489:685–698. doi:10.1051/0004-6361:200809633, 0807.0573

Ekström S, Georgy C, Eggenberger P, Meynet G, Mowlavi N, Wyttenbach A, Granada A, Decressin T, Hirschi R, Frischknecht U, Charbonnel C, Maeder A (2012) Grids of stellar models with rotation. I. Models from 0.8 to 120 solar masses at solar metallicity (Z = 0.014). Astron Astrophys 537:A146. doi:10.1051/0004-6361/201117751, 1110.5049

El Eid MF, Meyer BS, The LS (2004) Evolution of massive stars up to the end of central oxygen burning. Astrophys J 611:452–465. doi:10.1086/422162, arXiv:astro-ph/0407459

Eldridge JJ, Vink JS (2006) Implications of the metallicity dependence of Wolf-Rayet winds. Astron Astrophys 452:295–301. doi:10.1051/0004-6361:20065001, arXiv:astro-ph/0603188

Ertl T, Janka H-T, Woosley SE, Sukhbold T, Ugliano M (2016) A two-parameter criterion for classifying the explodability of massive stars by the neutrino-driven mechanism. Astrophys J 818:124. doi:10.3847/0004-637X/818/2/124

Fricke K (1968) Instabilität stationärer rotation in sternen. Zeitschrift fur Astrophysics 68:317

Frischknecht U, Hirschi R, Meynet G, Ekström S, Georgy C, Rauscher T, Winteler C, Thielemann FK (2010) Constraints on rotational mixing from surface evolution of light elements in massive stars. Astron Astrophys 522:A39. doi:10.1051/0004-6361/201014340, 1007.1779

Frischknecht U, Hirschi R, Thielemann FK (2012) Non-standard s-process in low metallicity massive rotating stars. Astron Astrophys 538:L2. doi:10.1051/0004-6361/201117794, 1112.5548

Frischknecht U, Hirschi R, Pignatari M, Maeder A, Meynet G, Chiappini C, Thielemann FK, Rauscher T, Georgy C, Ekström S (2016) S-process production in rotating massive stars at solar and low metallicities. Mon Not R Astron Soc 456:1803–1825. doi:10.1093/mnras/stv2723, 1511.05730

Georgy C, Meynet G, Maeder A (2011) Effects of anisotropic winds on massive star evolution. Astron Astrophys 527:A52. doi:10.1051/0004-6361/200913797, 1011.6581

Georgy C, Ekström S, Meynet G, Massey P, Levesque EM, Hirschi R, Eggenberger P, Maeder A (2012) Grids of stellar models with rotation. II. WR populations and supernovae/GRB progenitors at Z = 0.014. Astron Astrophys 542:A29. doi:10.1051/0004-6361/201118340, 1203.5243

Goldreich P, Schubert G (1967) Differential rotation in stars. Astrophys J 150:571

Gräfener G, Hamann WR (2008) Mass loss from late-type WN stars and its Z-dependence. Very massive stars approaching the Eddington limit. Astron Astrophys 482:945–960. doi:10.1051/0004-6361:20066176, 0803.0866

Heger A, Langer N (2000) Presupernova evolution of rotating massive stars. II. Evolution of the surface properties. Astrophys J 544:1016–1035. doi:10.1086/317239, arXiv:astro-ph/0005110

Heger A, Woosley SE (2010) Nucleosynthesis and evolution of massive metal-free stars. Astrophys J 724:341–373. doi:10.1088/0004-637X/724/1/341, 0803.3161

Heger A, Langer N, Woosley SE (2000) Presupernova evolution of rotating massive stars. I. Numerical method and evolution of the internal stellar structure. Astrophys J 528:368–396

Heger A, Fryer CL, Woosley SE, Langer N, Hartmann DH (2003) How massive single stars end their life. Astrophys J 591:288–300

Heger A, Woosley SE, Spruit HC (2005) Presupernova evolution of differentially rotating massive stars including magnetic fields. Astrophys J 626:350–363

Hirschi R (2004) Massive rotating stars: the road to supernova explosion. PhD Thesis. http://quasar.physik.unibas.ch/~hirschi/workd/thesis.pdf

Hirschi R (2007) Very low-metallicity massive stars: pre-SN evolution models and primary nitrogen production. Astron Astrophys 461:571–583. doi:10.1051/0004-6361:20065356, arXiv:astro-ph/0608170

Hirschi R, Maeder A (2010) The GSF instability and turbulence do not account for the relatively low rotation rate of pulsars. Astron Astrophys 519:A16. doi:10.1051/0004-6361/201014222, 1004.5470

Hirschi R, Meynet G, Maeder A (2004) Stellar evolution with rotation. XII. Pre-supernova models. Astron Astrophys 425:649–670

Hirschi R, Meynet G, Maeder A (2005) Yields of rotating stars at solar metallicity. Astron Astrophys 433:1013–1022. doi:10.1051/0004-6361:20041554, astro-ph/0412454

Hirschi R, Frischknecht U, Thielemann F, Pignatari M, Chiappini C, Ekström S, Meynet G, Maeder A (2008) Stellar evolution in the early universe. In: Hunt LK, Madden S, Schneider R (eds) IAU Symposium, vol 255, pp 297–304. doi:10.1017/S1743921308024976

Imbriani G, Limongi M, Gialanella L, Terrasi F, Straniero O, Chieffi A (2001) The $^{12}C(\alpha,\gamma)^{16}O$ Reaction rate and the evolution of stars in the mass range $0.8 \leq = M/M_{\odot} \leq 25$. Astrophys J 558:903–915. doi:10.1086/322288, arXiv:astro-ph/0107172

Jones S, Hirschi R, Nomoto K, Fischer T, Timmes FX, Herwig F, Paxton B, Toki H, Suzuki T, Martínez-Pinedo G, Lam YH, Bertolli MG (2013) Advanced burning stages and fate of 8-10 M stars. Astrophys J 772:150. doi:10.1088/0004-637X/772/2/150, 1306.2030

Käppeler F, Gallino R, Bisterzo S, Aoki W (2011) The s process: nuclear physics, stellar models, and observations. Rev Mod Phys 83:157–194. doi:10.1103/RevModPhys.83.157, 1012.5218

Kippenhahn R, Weigert A (1990) Stellar structure and evolution. Springer, New York

Kippenhahn R, Weigert A, Hofmeister E (1967) Methods for calculating stellar evolution. In: Alder B, Fernbach S, Rotenberg M (eds) Methods in computational physics, vol 7. Academic Press, New York/London

Knobloch E, Spruit HC (1983) The molecular weight barrier and angular momentum transport in radiative stellar interiors. Astron Astrophys 125:59–68

Krtička J, Owocki SP, Meynet G (2011) Mass and angular momentum loss via decretion disks. Astron Astrophys 527:A84. doi:10.1051/0004-6361/201015951, 1101.1732

Langer N (2012) Presupernova evolution of massive single and binary stars. Annu Rev Astron Astrophys 50:107–164. doi:10.1146/annurev-astro-081811-125534, 1206.5443

Langer N, Arcoragi JP, Arnould M (1989) Neutron capture nucleosynthesis and the evolution of 15 and 30 solar-mass stars. I. The core helium burning phase. Astron Astrophys 210: 187–197

Limongi M, Straniero O, Chieffi A (2000) Massive stars in the range 13–25 solar masses: evolution and nucleosynthesis. II. The solar metallicity models. Astrophys J Suppl Ser 129:625–664

Maeder A (1992) Stellar yields as a function of initial metallicity and mass limit for black hole formation. Astron Astrophys 264:105–120

Maeder A (1997) Stellar evolution with rotation. II. A new approach for shear mixing. Astron Astrophys 321:134–144

Maeder A (2003) Stellar rotation: evidence for a large horizontal turbulence and its effects on evolution. Astron Astrophys 399:263–269

Maeder A (2009) Physics, formation and evolution of rotating stars. Springer, Berlin/Heidelberg. doi:10.1007/978-3-540-76949-1

Maeder A, Meynet G (2000) Stellar evolution with rotation. VI. The Eddington and Omega-limits, the rotational mass loss for OB and LBV stars. Astron Astrophys 361:159–166

Maeder A, Meynet G (2001) Stellar evolution with rotation. VII. Low metallicity models and the blue to red supergiant ratio in the SMC. Astron Astrophys 373:555–571

Maeder A, Meynet G (2005) Stellar evolution with rotation and magnetic fields. III. The interplay of circulation and dynamo. Astron Astrophys 440:1041–1049. doi:10.1051/0004-6361:20053261

Maeder A, Meynet G (2012) Rotating massive stars: from first stars to gamma ray bursts. Rev Mod Phys 84:25–63. doi:10.1103/RevModPhys.84.25

Maeder A, Zahn J (1998) Stellar evolution with rotation. III. Meridional circulation with MU-gradients and non-stationarity. Astron Astrophys 334:1000–1006

Maeder A, Meynet G, Chiappini C (2015) The first stars: CEMP-no stars and signatures of spinstars. Astron Astrophys 576:A56. doi:10.1051/0004-6361/201424153, 1412.5754

Meynet G, Maeder A (1997) Stellar evolution with rotation. I. The computational method and the inhibiting effect of the {mu}-gradient. Astron Astrophys 321:465–476

Meynet G, Maeder A (2002a) Stellar evolution with rotation. VIII. Models at $Z = 10^{-5}$ and CNO yields for early galactic evolution. Astron Astrophys 390:561–583

Meynet G, Maeder A (2002b) The origin of primary nitrogen in galaxies. Astron Astrophys 381:L25–L28. doi:10.1051/0004-6361:20011554, astro-ph/0111187

Meynet G, Maeder A (2003) Stellar evolution with rotation. X. Wolf-Rayet star populations at solar metallicity. Astron Astrophys 404:975–990

Meynet G, Maeder A (2005) Stellar evolution with rotation. XI. Wolf-Rayet star populations at different metallicities. Astron Astrophys 429:581–598

Meynet G, Maeder A, Schaller G, Schaerer D, Charbonnel C (1994) Grids of massive stars with high mass loss rates. V. From 12 to 120 $M_\odot$ at $Z = 0.001, 0.004, 0.008, 0.020$ and 0.040. Astron Astrophys Suppl 103:97–105

Meynet G, Ekström S, Maeder A (2006) The early star generations: the dominant effect of rotation on the CNO yields. Astron Astrophys 447:623–639. doi:10.1051/0004-6361:20053070

Meynet G, Ekstrom S, Maeder A, Eggenberger P, Saio H, Chomienne V, Haemmerlé L (2013) Models of rotating massive stars: impacts of various prescriptions. In: Goupil M, Belkacem K, Neiner C, Lignières F, Green JJ (eds) Lecture notes in physics, vol 865. Springer, Berlin, pp 3–642, 1301.2487

Muijres LE, de Koter A, Vink JS, Krtička J, Kubát J, Langer N (2011) Predictions of the effect of clumping on the wind properties of O-type stars. Astron Astrophys 526:A32. doi:10.1051/0004-6361/201014290

Ness M, Asplund M, Casey AR (2014) NGC 6522: a typical globular cluster in the galactic bulge without signatures of rapidly rotating population III stars. Mon Not R Astron Soc 445:2994–2998. doi:10.1093/mnras/stu2144, 1408.0290

Nishimura N, Hirschi R, Pignatari M, Herwig F, Beard M, Imbriani G, Görres J, deBoer RJ, Wiescher M (2014) Impact of the uncertainty in α-captures on ^{22}Ne on the weak s-process in massive stars. In: Jeong S, Imai N, Miyatake H, Kajino T (eds) American institute of physics conference series, vol 1594, pp 146–151. doi:10.1063/1.4874059

Nomoto K (1984) Evolution of 8-10 solar mass stars toward electron capture supernovae. I. Formation of electron-degenerate O + NE + MG cores. Astrophys J 277:791–805. doi:10.1086/161749

Nomoto K (1987) Evolution of 8-10 solar mass stars toward electron capture supernovae. II. Collapse of an O + NE + MG core. Astrophys J 322:206–214. doi:10.1086/165716

Nugis T, Lamers HJGLM (2000) Mass-loss rates of Wolf-Rayet stars as a function of stellar parameters. Astron Astrophys 360:227–244

O'Connor E, Ott CD (2011) Black hole formation in failing core-collapse supernovae. Astrophys J 730:70. doi:10.1088/0004-637X/730/2/70, 1010.5550

Paxton B, Bildsten L, Dotter A, Herwig F, Lesaffre P, Timmes F (2011) Modules for experiments in stellar astrophysics (MESA). Astrophys J Suppl Ser 192:3. doi:10.1088/0067-0049/192/1/3, 1009.1622

Pignatari M, Gallino R (2008) The weak s-process at low metallicity. In: O'Shea BW, Heger A (eds) First stars III, american institute of physics conference series, vol 990, pp 336–338. doi:10.1063/1.2905575

Pignatari M, Gallino R, Meynet G, Hirschi R, Herwig F, Wiescher M (2008) The s-process in massive stars at low metallicity: the effect of primary ^{14}N from fast rotating stars. Astrophys J Lett 687:L95–L98. doi:10.1086/593350, 0810.0182

Pignatari M, Gallino R, Heil M, Wiescher M, Käppeler F, Herwig F, Bisterzo S (2010) The weak s-process in massive stars and its dependence on the neutron capture cross sections. Astrophys J 710:1557–1577. doi:10.1088/0004-637X/710/2/1557

Pignatari M, Hirschi R, Wiescher M, Gallino R, Bennett M, Beard M, Fryer C, Herwig F, Rockefeller G, Timmes FX (2013) The $^{12}\mathrm{C} +^{12}\mathrm{C}$ Reaction and the impact on nucleosynthesis in massive stars. Astrophys J 762:31. doi:10.1088/0004-637X/762/1/31, 1212.3962

Poelarends AJT, Herwig F, Langer N, Heger A (2008) The supernova channel of super-AGB stars. Astrophys J 675:614–625. doi:10.1086/520872, 0705.4643

Potter AT, Chitre SM, Tout CA (2012) Stellar evolution of massive stars with a radiative α-Ω dynamo. Mon Not R Astron Soc 424:2358–2370. 1205.6477

Prantzos N, Hashimoto M, Nomoto K (1990) The s-process in massive stars – yields as a function of stellar mass and metallicity. Astron Astrophys 234:211–229

Pumo ML, Contino G, Bonanno A, Zappalà RA (2010) Convective overshooting and production of s-nuclei in massive stars during their core He-burning phase. Astron Astrophys 524:A45. doi:10.1051/0004-6361/201015518, 1009.5333

Raiteri CM, Busso M, Picchio G, Gallino R (1991) S-process nucleosynthesis in massive stars and the weak component. II. Carbon burning and galactic enrichment. Astrophys J 371:665–672. doi:10.1086/169932

Raiteri CM, Gallino R, Busso M (1992) S-processing in massive stars as a function of metallicity and interpretation of observational trends. Astrophys J 387:263–275. doi:10.1086/171078

Rauscher T, Heger A, Hoffman RD, Woosley SE (2002) Nucleosynthesis in massive stars with improved nuclear and stellar physics. Astrophys J 576:323–348

Rayet M, Hashimoto M (2000) The s-process efficiency in massive stars. Astron Astrophys 354:740–748

Ritossa C, García-Berro E, Iben I Jr (1999) On the evolution of stars that form electron-degenerate cores processed by carbon burning. V. Shell convection sustained by helium burning, transient neon burning, dredge-out, URCA cooling, and other properties of an 11 M_solar population I model star. Astrophys J 515:381–397. doi:10.1086/307017

Smartt SJ (2009) Progenitors of core-collapse supernovae. Annu Rev Astron Astrophys 47:63–106. doi:10.1146/annurev-astro-082708-101737, 0908.0700

Spruit HC (2002) Dynamo action by differential rotation in a stably stratified stellar interior. Astron Astrophys 381:923–932

Sukhbold T, Woosley SE (2014) The compactness of presupernova stellar cores. Astrophys J 783:10. doi:10.1088/0004-637X/783/1/10, 1311.6546

Sylvester RJ, Skinner CJ, Barlow MJ (1998) Silicate and hydrocarbon emission from galactic M supergiants. Mon Not R Astron Soc 301:1083–1094. doi:10.1046/j.1365-8711.1998.02078.x

Takahashi K, Yoshida T, Umeda H (2013) Evolution of progenitors for electron capture supernovae. Astrophys J 771:28. doi:10.1088/0004-637X/771/1/28, 1302.6402

The LS, El Eid MF, Meyer BS (2000) A new study of s-process nucleosynthesis in massive stars. Astrophys J 533:998–1015. doi:10.1086/308677

The LS, El Eid MF, Meyer BS (2007) s-process nucleosynthesis in advanced burning phases of massive stars. Astrophys J 655:1058–1078. doi:10.1086/509753, arXiv:astro-ph/0609788

Thielemann FK, Arnett WD (1985) Hydrostatic nucleosynthesis – part two – core neon to silicon burning and presupernova abundance yields of massive stars. Astrophys J 295:604

Travaglio C, Gallino R, Arnone E, Cowan J, Jordan F, Sneden C (2004) Galactic evolution of Sr, Y, and Zr: a multiplicity of nucleosynthetic processes. Astrophys J 601:864–884. doi:10.1086/380507, arXiv:astro-ph/0310189

Tur C, Heger A, Austin SM (2009) Dependence of s-process nucleosynthesis in massive stars on triple-alpha and $^{12}\mathrm{C}(\alpha,\gamma)^{16}\mathrm{O}$ reaction rate uncertainties. Astrophys J 702:1068–1077. doi:10.1088/0004-637X/702/2/1068, 0809.0291

Umeda H, Nomoto K (2005) Variations in the abundance pattern of extremely metal-poor stars and nucleosynthesis in population III supernovae. Astrophys J 619:427–445. doi:10.1086/426097

van Loon JT, Groenewegen MAT, de Koter A, Trams NR, Waters LBFM, Zijlstra AA, Whitelock PA, Loup C (1999) Mass-loss rates and luminosity functions of dust-enshrouded AGB stars and red supergiants in the LMC. Astron Astrophys 351:559–572, arXiv:astro-ph/9909416

van Loon JT, Cioni MRL, Zijlstra AA, Loup C (2005) An empirical formula for the mass-loss rates of dust-enshrouded red supergiants and oxygen-rich asymptotic giant branch stars. Astron Astrophys 438:273–289. doi:10.1051/0004-6361:20042555, arXiv:astro-ph/0504379

Vink JS, de Koter A, Lamers HJGLM (2001) Mass-loss predictions for O and B stars as a function of metallicity. Astron Astrophys 369:574–588. doi:10.1051/0004-6361:20010127

Vink JS, Gräfener G, Harries TJ (2011) In pursuit of gamma-ray burst progenitors: the identification of a sub-population of rotating Wolf-Rayet stars. Astron Astrophys 536:L10. doi:10.1051/0004-6361/201118197, 1111.5806 von Zeipel H (1924) The radiative equilibrium of a rotating system of gaseous masses. Mon Not R Astron Soc 84:665

Walder R, Folini D, Meynet G (2011) Magnetic fields in massive stars, their winds, and their nebulae. Space Sci Rev 125. doi:10.1007/s11214-011-9771-2, 1103.3777

Wiescher M, Käppeler F, Langanke K (2012) Critical reactions in contemporary nuclear astrophysics. Annu Rev Astron Astrophys 50:165–210. doi:10.1146/annurev-astro-081811-125543

Woosley SE, Heger A (2006) The progenitor stars of gamma-ray bursts. Astrophys J 637:914–921. doi:10.1086/498500

Woosley SE, Heger A (2015) The remarkable deaths of 9-11 solar mass stars. Astrophys J 810:34. doi:10.1088/0004-637X/810/1/34, 1505.06712

Yoon SC, Langer N (2005) Evolution of rapidly rotating metal-poor massive stars towards gamma-ray bursts. Astron Astrophys 443:643–648. doi:10.1051/0004-6361:20054030

Yoon SC, Langer N, Norman C (2006) Single star progenitors of long gamma-ray bursts. I. Model grids and redshift dependent GRB rate. Astron Astrophys 460:199–208. doi:10.1051/0004-6361:20065912, arXiv:astro-ph/0606637

Yusof N, Hirschi R, Meynet G, Crowther PA, Ekström S, Frischknecht U, Georgy C, Abu Kassim H, Schnurr O (2013) Evolution and fate of very massive stars. Mon Not R Astron Soc 433:1114–1132. doi:10.1093/mnras/stt794, 1305.2099

Zahn J, Brun AS, Mathis S (2007) On magnetic instabilities and dynamo action in stellar radiation zones. Astron Astrophys 474:145–154. doi:10.1051/0004-6361:20077653, 0707.3287

Zahn JP (1992) Circulation and turbulence in rotating stars. Astron Astrophys 265:115–132